Deep Learning-Based PET Image Correction Toward Quantitative Imaging

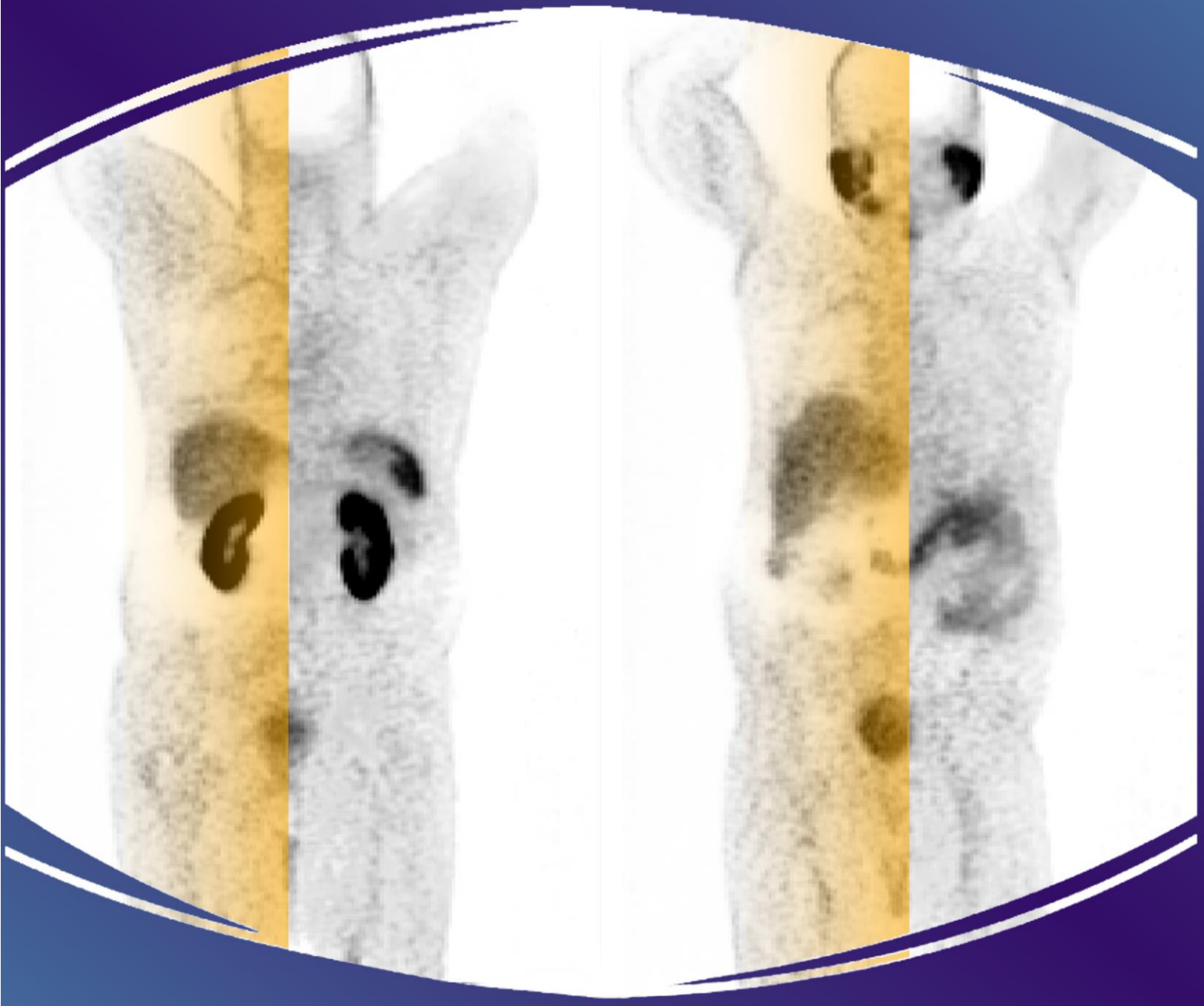

Zohreh Shahpouri

460145

Data Science for life Science

June 01, 2024

Dr. Isaac Shiri Lord

INSELGRUPPE

Deep Learning-Based PET Image Correction Toward Quantitative Imaging

Author

Zohreh Shahpouri

Student number

460145

Study

Data Science for Life Science

Institute

Hanze University of Applied Sciences

Institute of Life Science & Technology

Supervisor

Dr. Isaac Shiri Lord

Abstract

Recent advancements in deep learning (DL) offer significant advantages in PET imaging, particularly in enhancing attenuation scatter correction (ASC) and artifact removal. However, practical implementation remains challenging due to variability in scanner types and radiotracer distributions. We aim to develop an Integrated Multi-Center DL Model (IMCM) to address the direct ASC of PET images and evaluate its performance in removing image artifacts.

A total of 270 clean and artifact-free images were selected from a collection of over 2000 patient images undergoing ^{68}Ga and ^{18}F-FDG PET/CT scans across seven centers. Three centers were designated for external testing: one for ^{68}Ga data (Cross-Center) and two for ^{18}F-FDG data (Cross-Tracer). A dedicated 3D-UNet model employing a deep supervision strategy was trained on artifact-free images from four centers. The model's performance was then evaluated quantitatively and qualitatively for artifact correction on three external test sets.

For the internal centers, the IMCM model achieved a Mean Error (ME) of -0.56±0.74, a Mean Absolute Error (MAE) of 1.28±0.37, and a Structural Similarity Index (SSIM) of 0.93±0.03. For the external test sets, IMCM yielded an ME of -1.92±0.58 and -0.54±0.13, an MAE of 2.38±0.76 and 0.69±0.12, and an SSIM of 0.89±0.03 and 0.78±0.10 for the Cross-Center and Cross-Tracer, respectively. IMCM successfully corrected motion and halo artifacts in both ^{68}Ga data and ^{18}F-FDG images.

The developed model effectively addressed variations in scanner types and radiotracers, demonstrating its adaptability, generalizability, and effectiveness in different clinical scenarios for direct ASC and artifact correction. This study highlighted the potential of DL to provide accurate, artifact-free PET images, offering a promising alternative to CT-based ASC.

Keywords: Deep learning, attenuation scatter correction, CT-less PET.

Abbreviation

Positron Emission Tomography	PET
Magnetic Resonance Imaging	MRI
Attenuation correction	AC
Attenuation and scatter correction	ASC
Computed Tomography	CT
Gallium-68	^{68}Ga
Fluorodeoxyglucose	FDG
Non attenuation scatter correction	NAC
CT based attenuation-scatter correction	MAC
Time of flight	TOF
Maximum likelihood estimation of activity and attenuation	MLAA
Long axial field of view	LAFOV
Artificial Intelligent	AI
Federated learning	FL
Prostate-Specific Membrane Antigen	PSMA
Anatomy-dependent correction model	ADCM
Deep learning model-based attenuation correction	DL
Standard uptake value	SUV
Integrated multi-Center model	IMCM
Tuned Transfer Learning for IMCM model	TL-MC

Table of Contents

Introduction

Positron Emission Tomography (PET) is the gold standard of molecular imaging modalities for the non-invasive study of various diseases (1–3). Numerous patients undergo PET scans worldwide for staging and restaging cancer, evaluating treatment diagnostic, radiation therapy planning, diagnosing neurological disorders, Assessing myocardial perfusion, and surgical planning (4–6).

During a whole-body PET image creation, more than 50% of all recorded photons result in a Compton scatter fraction before capturing by detectors (7–9). Photon scattering occurs due to dense materials in the patient's body and surrounding area and causes energy loss. A misplaced line of response (LOR) is formed by a scattered, attenuated photon, which has not been declined after energy window discrimination and random coincidence correction technique (10). So, scatter and attenuation phenomena lead to miscalculation of radiopharmaceutical distribution inside the body (7,10).Attenuation and Scatter correction (ASC) has a critical role in achieving a high-quality image interpretation and acceptable quantitative analysis of PET scans (Figure 1) (11,12). ASC was performed using a CT scanner to model attenuation coefficient maps (μ-maps). Typically, an unenhanced, low-dose CT scan is conducted alongside PET scans for ASC, and occasionally, a diagnostic CT scan with a contrast agent may serve the same function (13,14).

While various research has been done to create μ-maps from proton density information, ASC has remained a challenge in Magnetic Resonance Imaging (MRI) based AC. Despite the implementation of CT or MRI for ASC, artifacts, which are anomalies in the final images and do not correspond to the authentic radiotracer distribution within the body, can still occur (15–18). Patient motion during or between two scans complicates the alignment of PET with CT or MR images, causes mismatch, misregistration, or motion artifacts (15,16,19,20). Moreover, in reconstruction with ASC, neighboring areas to high-activity organs, such as the kidney bladder, might assign negative or zero values, leading to halo artifacts in clinical observations (21,22).

Halo artifacts are very common in ^{68}Ga-PET imaging, which is widely used for prostate and pelvic cancer diagnosis, staging, and treatment planning. This artifact might change the quantitative interpretation of clinical diagnosis. To remove these artifacts, like giving diuretics, often makes the patient more uncomfortable and increases the chance of motion artifacts, which makes the image quality and readability even worse (23,24).

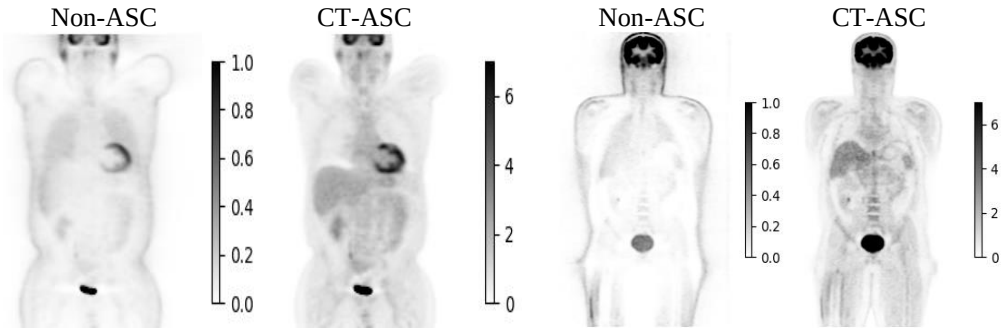

Figure 1: showcases examples of PET images before and after attenuation and scatter correction.

Most PET acquisition settings are performed with arms up (to decrease photon scatter). As arm raising is uncomfortable for patients, this will cause arm motion during sequential PET and CT/MRI scans (25–27). The presence of artifacts can significantly decrease the image quality and accuracy of interpretation and result in misdiagnoses. Consequently, even repeating scans fails to resolve the issue and can lead to an increased cumulative total body dose, higher utilization rates, and longer waiting times (28–30).

Overall, this field has seen progress through different algorithms for generating μ-maps, such as the maximum likelihood estimation of activity and attenuation (MLAA), which is limited by insufficient coincidence time. Further, MLAA and similar algorithms are enhanced in combination with time of flight (TOF) (31–33)(34). Further enhancement on MLAA and similar algorithms is done in combination with time of flight (TOF). Whole-body PET scanners with a long axial field of view (LAFOV) have significantly improved quantification and image resolution (8,9,35–38). However, up until now, the relationship between activity distribution and attenuation is a challenging frontier (28). Recent notable progress in segmentation, classification, detection, noise reduction, and reconstruction research areas utilizing artificial intelligence (AI) has encouraged nuclear medicine researchers to investigate CT-free methods for ASC in PET imaging (39–58). CT Elimination has advantages for those who require repeated scans, especially for pediatric patients, as even a minor reduction in cumulative radiation exposure could cause a significant impact (59,60).

Some Deep Learning-based methods have been developed to generate the synthesis of pseudo-CT images from MRI or uncorrected PET data, prediction of scatter maps from emission data (61–66), while other research focuses on the direct generation of ASC PET images from non-attenuation-scatter-correction (NAC) as inputs to predict ASC PET images directly (40,44,67). The direct image-to-image translation technique not only highlights the capabilities of deep learning models in ASC without CT but also possesses the ability to detect and correct artifacts in PET images accurately (68,69).

An important question facing researchers today is the practical applicability of these models in clinical environments. Due to differences in spatial resolution, sensitivity, and technical information among scanners and variations of radiotracer biodistribution in the body, a model optimized for data from one specific scanner may not perform effectively under different conditions or other equipment. Moreover, not all medical centers are equipped with a dedicated AI team or even restricted in data sharing by ethical and regulatory considerations. Federated learning (FL) addresses some challenges, such as data privacy and limited dataset sizes in medical imaging (17,18,70,71). Yet, to achieve widespread clinical acceptance and enhance PET imaging's diagnostic capabilities, novel correction techniques in CT-free PET imaging avenues must be sought.

Previous research has shown that direct ASC frameworks can correct artifacts in ^{18}F-FDG PET/CT images (66). Additionally, the GAN model's performance in combination with ^{68}Ga and ^{18}F radiotracers across various centers has been evaluated (39). Additionally, the detection and correction of ^{18}Ga image artifacts using a tuned direct ASC model for multiple centers have been assessed. Despite these advances, further investigation into a multi-center model for quantitative analysis of gallium studies is still needed.

The main aim of this study is to address the direct ASC of PET images and evaluate its performance in removing image artifacts using the multicenter dataset. We will use our approach to estimate and compare the performance of models using both strategies within different radiotracers and scanners. In particular, we will integrate domain expertise into our deep learning framework to detect and correct artifacts more efficiently in multi-center studies.

Material and methods

Data Preparation

^{68} Ga PET/CT scans from five different hospitals from the previous study were used for training and initial model validation in the primary stage of this study (18). A secondary dataset, distinct in both the imaging centers and the type of radiotracer used (^{18}F-FDG PET scans from two different hospitals), was incorporated to test the model's adaptability. Additionally, a specialized set of images presenting artifacts was included to assess the model's capability to detect and correct image quality issues.

^{68}Ga PET/CT dataset

A cohort of 1000 patients underwent ^{68}Ga-prostate-specific membrane antigen (PSMA). PET/CT imaging across five centers located in different countries. To ensure the integrity of the data for model training, an expert in nuclear medicine evaluated all the scans, identifying 184 images of optimal quality without artifacts from the total pool. Detailed information on the datasets collected is outlined in Table 1. The CT-based ASC was applied to amend PET images for accurate correction of attenuation and scatter effects on the images. For this study, non-attenuation-corrected images will be referred to as NAC, and CT-based attenuation scatter-corrected images will be denoted as MAC.

Table 1: Data information in 5 different imaging centers.

Center	No	Train	Validation	Test	Scanner	Reconstruction	Matrix size × Z*
Center 1	56	43	11	2	Siemens Biograph 6	3D-OSEM	168 × 168
Center 2	31	25	4	2	GE Discovery IQ	3D-OSEM	192 × 192
Center 3	45	35	8	2	Siemens mCT	3D-OSEM	200 × 200
Center 4	40	28	10	2	Siemens Biograph 6	3D-OSEM	168 × 168
External Center	12	-	-	12	Siemens Horizon	PSF+TOF+3D-OSEM	180 × 180
Total	184	131	33	20	-	-	-
* Z' representing the number of slices in the axial view, depends on body length, scanner resolution, scan protocol, and patient positioning. So, it is different patiently.							

Normalization of PET Image

The standard uptake value (SUV) in PET imaging is an important standardization procedure that allows quantitative measurement. This means that the detected radiotracer concentration reflects the metabolism of the patient's body. It corrects based on the radiotracer injected dose and the patient's body weight. This conversion is essential as it factors in variations due to patient size and the amount of radiotracer administered. The SUV is calculated using the Equation 1:

$$\mathrm{SUV} = \frac{\text{Voxel Activity Concentration}_{(\mathrm{Bq/ml})}}{\text{Injected Dose}_{(\mathrm{Bq})} \Big/ \text{Body Weight}_{(\mathrm{kg})}} \qquad (1)$$

To turn the voxel values into SUV metrics, this conversion was done the same way on all MAC and NAC images. To preserve quantitative values across all images and since deep learning models operate more efficiently with smaller numbers, the images were normalized by dividing them by a constant factor. MAC images underwent a factor of 5 scaling, while 2 was picked for NAC images.

This method of normalization ensures that the data remains quantitatively comparable while being computationally straightforward. By scaling the intensity values in this manner, we were able to preserve the quantitative nature of PET imaging and easily rescale the images back to the original, which is vital for accurate diagnosis and assessment of metabolic activity. The histogram of the images post-normalization illustrates the effect of this scaling on the distribution of voxel intensities, confirming the consistency of intensity levels across the processed images (Figure 2A).

Data Transformation and Augmentations:

For training data preparation, each PET image was initially trimmed to fit the body's outline, followed by the addition of zero-padding to standardize the dimensions to a uniform bounding box size of 168×168×Z (with 'Z' representing the count of slices), as illustrated in Figure 2a. This ensured the retention of the original image resolution and anatomical structure. To ensure uniformity and enhance the training process's efficiency, all PET images were re-scaled to a voxel size of 4.07 × 4.07 × 3.0 mm^3, the most common resolution across the collected data and crucial for consistent image analysis. This standardization was crucial for achieving consistent image quality throughout the dataset. Details regarding the initial voxel spacing are provided in Figure 2b.

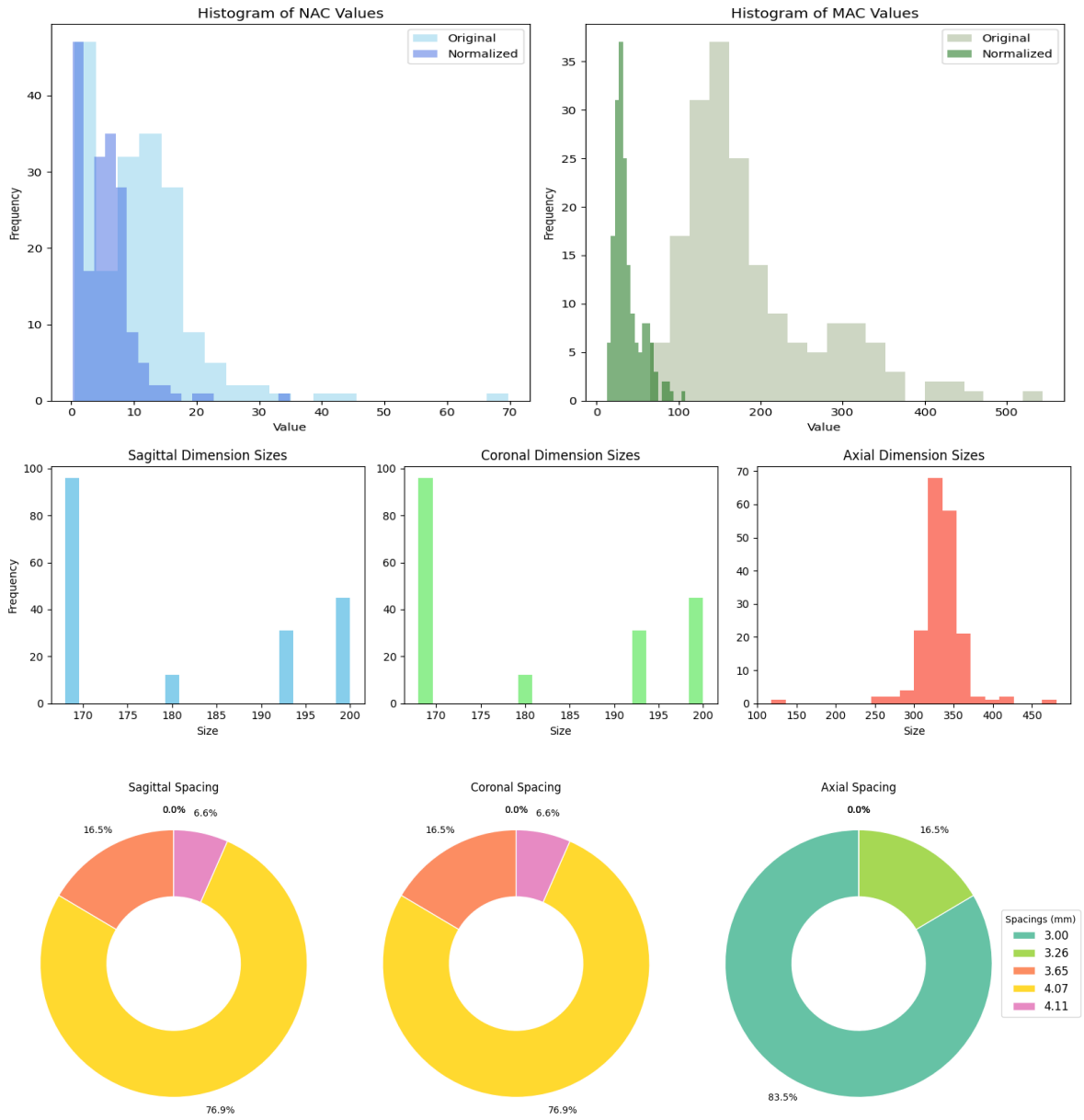

Figure 2: ***A)*** *Distribution of maximum intensity values for NAC and MAC images, displaying variations pre- and post-normalization to highlight data scaling effects. NAC images were scaled down by a factor of 2 and MAC images by a factor of 5.* ***B)*** *initial PET image dimensions are distributed across sagittal, coronal, and axial planes. Each bar represents the frequency of occurrence for specific dimension sizes within the dataset.* ***C)*** *Proportion of different voxel spacings utilized in PET image preprocessing. The donut charts depict the percentage of images corresponding to each voxel spacing dimension in millimeters across sagittal, coronal, and axial views.*

Generation of Anatomy-Dependent Correction Maps (ADCM)

In exploring advanced techniques for PET image correction, we examine a decomposition-based deep learning approach previously proposed (39). From NAC to MAC, the complex MAC was divided into two parts: anatomy-independent textures (related to tracers and diseases) and anatomy-dependent correction. In other words, this method involves dividing the MAC image into these two key component maps. Anatomy-independent information, which correlates with tracer type and disease pathology, and another component, anatomy-dependent factors necessary for image correction.

The anatomy-dependent correction map (ADCM) at each voxel is defined by conditional Equation 2, which captures the ratio of the MAC intensity to the NACs:

$$If\ PET_{NAC}[x,y,z]\ \geq\ \varepsilon\ then$$

$$PET_{ADCM}[x,y,z]\ =\ {PET_{NAC}[x,y,z]}\Big/{PET_{NAC}[x,y,z]} \qquad (2)$$

$$else\quad PET_{ADCM}[x,y,z]\ =\ PET_{MAC}[x,y,z]$$

The threshold ε ensures that division by zero is avoided, defaulting to the MAC intensity where necessary.

In the evaluation phase, our trained model predicts the DL-ADCM for a given NAC. We then employ the following transformation (Equation 3) to achieve the DL model-based attenuation correction (DL):

$$If\ PET_{NAC}[x,y,z]\ >\ \varepsilon\ then$$

$$PET_{DL}[x,y,z]\ =\ PET_{NAC}[x,y,z]\ *\ PET_{DL-ADCM}[x,y,z] \qquad (3)$$

$$else\ PET_{DL}[x,y,z]\ =\ PET_{NAC}[x,y,z]$$

Sample cases are visualized in Figure 3.

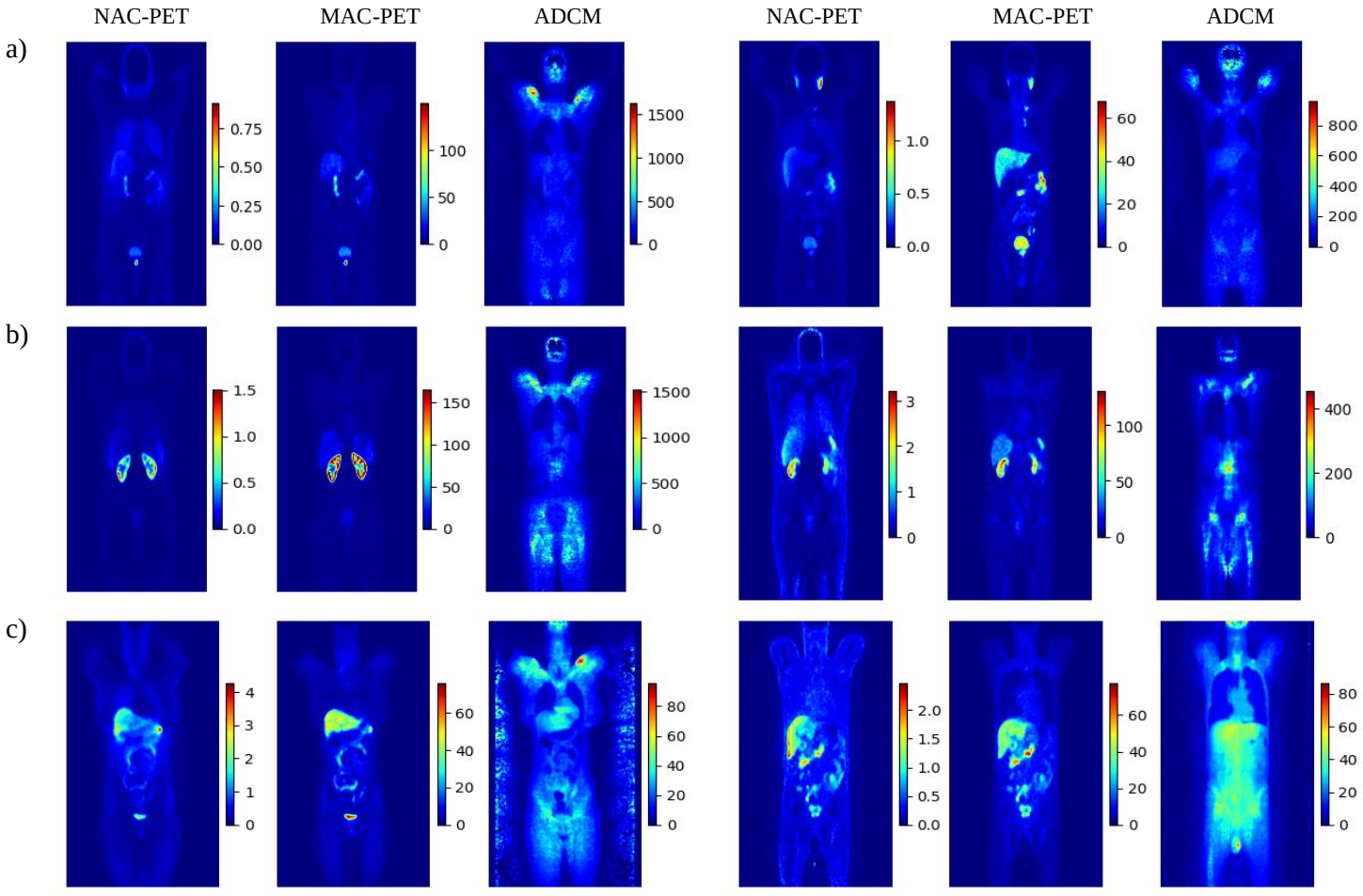

Figure 3: The middle slice of the coronal view for NAC, MAC, and ADCM images. Color bar unit: SUV

Normalization of ADCM

As we already mentioned, famous normalization methods were not used to calibrate ADCM to preserve the quantitative accuracy of SUV, which is necessary for accurate clinical interpretations. We came up with an empirical normalization factor just for ADCM values. This factor was carefully chosen to make the dataset's wide range of values more manageable. This factor ensures the broad spectrum of data, ranging from minimal to several thousand units, is normalized to permit later recalibration into their original SUV metrics. Notably, extreme values that could bias the model (such as outliers with values of 28180 and 7300) were carefully excluded to align the focus with the representative range critical for analysis. Then, voxel intensities were normalized using a factor of 50 to maintain relative, comparable, and manageable values for training. The resultant histograms, illustrating the distribution of maximum values both pre- and post-normalization, are depicted in Figure 5.

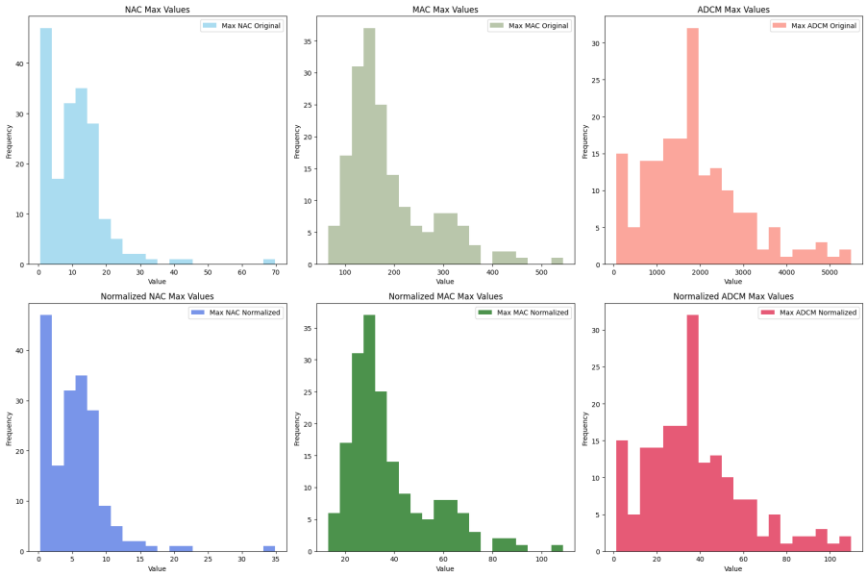

Figure 4: shows the range of highest intensity values for NAC and MAC images as well as ADCM metrics, showing changes before and after normalization to show how data scaling affects the images. NAC images are scaled down by a factor of 2, MAC images by a factor of 5, and ADCM by a factor of 50.

^{18}F-FDG Datasets

To assess the model's performance with different radiotracers, our study incorporated a dataset of 98 whole-body ^{18}F-FDG PET scans originating from two distinct centers, representing our external radiotracer dataset (Figure 6). During the preprocessing phase, the intensities of voxels in both MAC and NAC images were standardized for SUVs by scaling factors, 9 for MAC and 3 for NAC images.

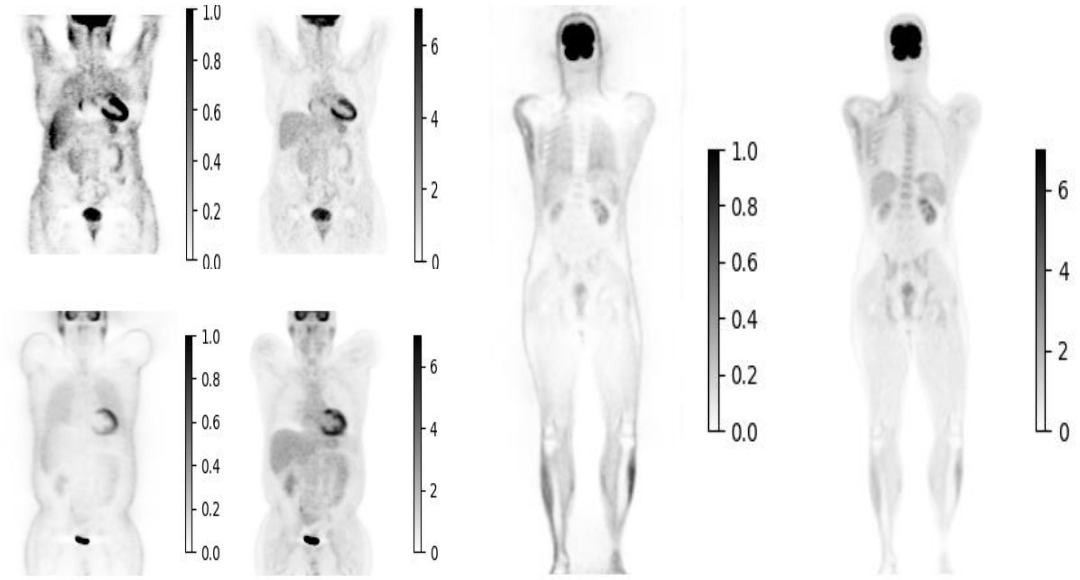

Figure 5: Sample of coronal slices from an FDG dataset, illustrating the range in axial slice counts, which vary from 180 to 600 based on the organ of interest.

Table 2: "Overview of External Radiotracer Dataset Specifications.

Center	No	Train	Validation	Test	Matrix size × Z
Center 6	55	39	6	11	272 × 200
Center 7	43	23	9	10	272 × 200
Total	98	62	15	21	-
* Z' representing the number of slices in the axial view, depends on body length, scanner resolution, scan protocol, and patient positioning. So, it is different patiently.					

Artifact dataset

A third test set was utilized to evaluate the performance of the developed model under more challenging conditions. This set consisted of imaging data from 198 patients, each displaying various types of artifacts. The artifacts in this dataset were chosen to test how well the model can handle and correctly interpret images that are distorted by common problems seen in clinical ^{18}Ga imaging, like motion and Halo artifacts.

Deep neural network

For final implementation, we used the Dyn-UNet architecture, renowned for its adaptability and efficiency in processing biomedical images (72)This model is chosen for its dynamic configuration and deep supervision, which enable precise results tailored to the specific requirements of our dataset. The Dyn-UNet model's initialization is specially made to find the best kernel sizes and strides based on the size and spacing of the input patches in our dataset. These parameters were determined by evaluating the spatial dimensions and resolution of the input data, ensuring the network architecture is directly aligned with the inherent characteristics of our medical images.

The Dyn-UNet model is specified with supervision heads, which ensure that intermediate layers are optimized for accurate prediction, enhancing learning efficiency and model robustness. Deep supervision ensures that intermediate layers are also optimized for accurate prediction, not just the final

output layer. This strategy boosts the learning efficiency and enhances the robustness of the model, making it adept at segmenting complex anatomical structures with high fidelity.

For the ^{68}Ga dataset, the computed kernel sizes and strides are set to four layers of [3, 3, 3] kernels, with strides transitioning from [1, 1, 1] in the initial layer to [2, 2, 1] in the deeper layers. Additionally, the implementation of deep supervision, with two supervision heads, enhanced the learning process by optimizing the network's final and intermediate layers. By adjusting the ReLU activation function in the last layer, we can get the non-zero value for the concept of the PET image. Our deep learning network was designed to process NAC images as inputs to generate MAC or ADCM images for different approaches and will be elaborated upon later.

Network training involved using 3D patches sized at 168×168×16 and 20 sample patches per patient. The key training parameters were as follows: Learning rate of 0.001, Loss function of the mean squared error (MSE)—also referred to as the squared L2 norm. The MSE loss function was employed to measure the deviation of the network's output from the MAC ground truth.

The network was optimized using the Adam algorithm. The beta coefficients, set at 0.5 and 0.999, governed the moment estimates' exponential decay rates. Supplemental Material 1 details the architecture and more information about this network. Only artifact-free datasets were used during the network's training and validation stages to maintain the model's integrity. We trained the network near 500 epochs to ensure adequate convergence and comprehensive learning from the dataset. To prevent data leakage and ensure data integrity, patients were not overlapped across the training, testing, and validation datasets, maintaining the independence of each dataset. Details on alternative models tested, including those that did not meet our criteria for inclusion in the final report, are documented in Supplementary Material 1 for transparency and completeness.

Training approaches for deep learning models:

Integrated multi-center model (IMCM):

A Dyn-Unet deep learning model was developed using a combined dataset from four different centers, all utilizing ^{68}Ga-based radiotracers. This model was initially trained on a collective dataset and subsequently tested on an external center’s data to evaluate its generalization capabilities. It was also tested within the originating dataset from each center. This approach aims to overcome the limitations of models trained on data from single centers, which may struggle with generalizability to new, unseen cases. The training and validation losses for the IMCM are illustrated in Figure 7.

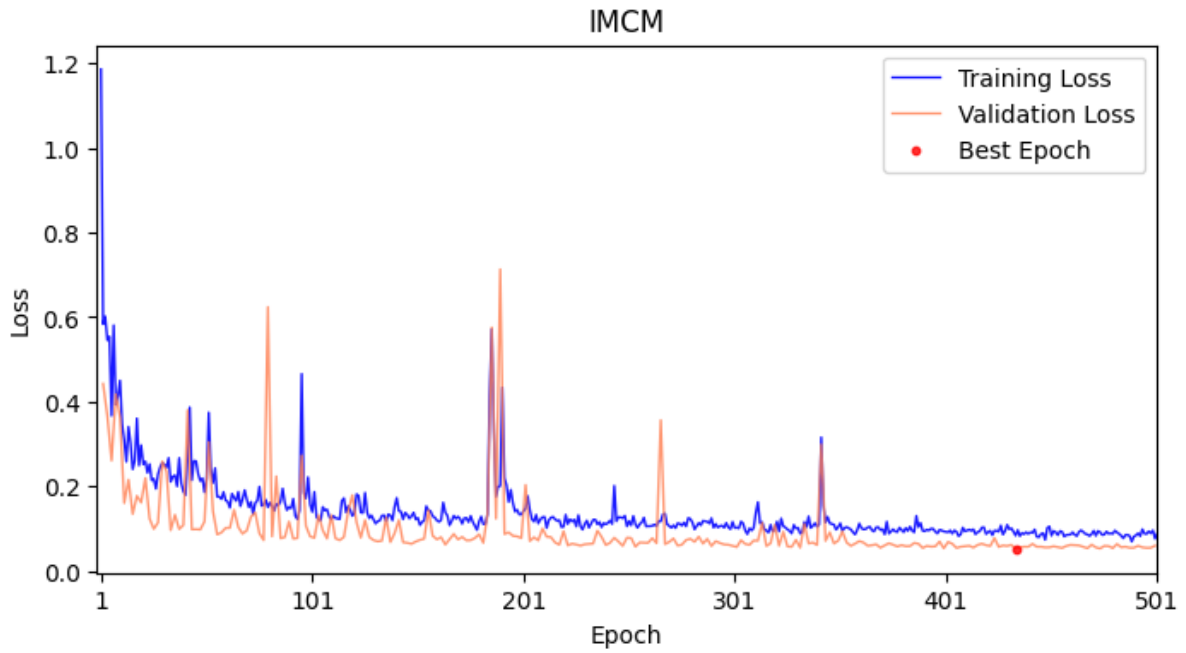

Figure 6: Training and validation loss for the Integrated Multi-Center Model showing the best metric of 0.0527 at epoch 434.

Anatomy-Dependent Correction Model (ADCM):

This methodology adopts a new approach by decomposing the transformation from non-attenuation-corrected PET (NAC-PET) to model-based attenuation-corrected PET (MAC-PET) into two distinct components. Specifically, the model targets anatomy-independent features associated with tracers and diseases and anatomy-dependent corrections that are crucial for accurate image interpretation. This decomposition enables more targeted and efficient data handling during the deep learning process.

The previous network focused exclusively on estimating the anatomy-dependent correction maps (ADCM). This model's effectiveness is evaluated through its ability to generalize across different centers and tracers, testing its robustness in a variety of clinical settings. The training progress and validation stability for the ADCM are detailed in Figure 8.

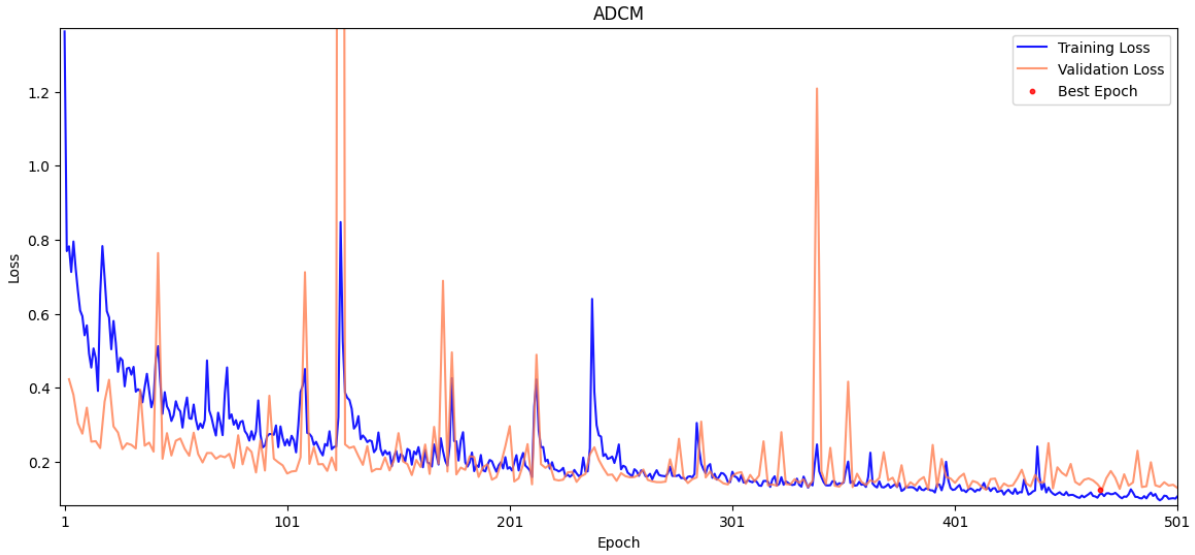

Figure 7: Training and validation loss for the ADCM model, where the best metric of 0.1237 was reached at epoch 466.

Tuned Transfer Learning for IMCM model (TL-MC):

The IMCM model underwent tuning through transfer learning (TL) to address the challenges encountered with different radiotracers. This method involves modifying the deep learning model by integrating learning with the new dataset. This refinement enhanced the model's performance and adaptability across different tracer types, providing a more robust solution that could potentially handle variability more effectively. The effectiveness of the TL approach is depicted in Figure 9, demonstrating rapid convergence and effective transfer learning.

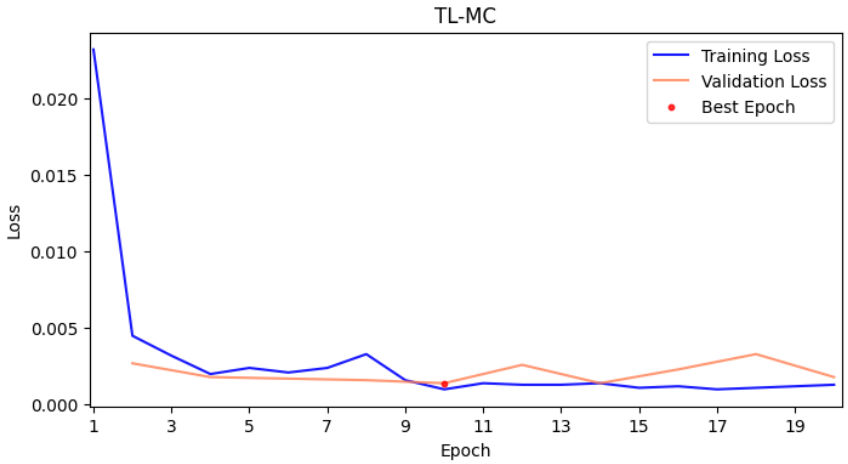

Figure 8: Training and validation loss for the Tune TL Model with a best metric of 0.0014 achieved at epoch 10, demonstrating rapid convergence and effective transfer learning.

Quantitative evaluation:

The model's efficacy was rigorously quantified using a range of statistical metrics, calculated by comparing the DL-predicted PET images against the ground truth CT-based attenuation/scatter-corrected images. These voxel-wise metrics are computed as follows:

- **Mean Error (ME):** This reflects the average deviation across all voxels.

$$ME = \frac{1}{tot} \sum_{v=1}^{tot} PET_{pred}(v) - PET_{ref}(v) \quad (4)$$

- **Mean Absolute Error (MAE):** Measures the average magnitude of errors without considering their direction.

$$MAE = \frac{1}{tot} \sum_{v=1}^{tot} \left| PET_{pred}(v) - PET_{ref}(v) \right| \quad (5)$$

- **Relative Error (RE%):** Provides a percentage error relative to the true values, indicating the proportion of the deviation.

$$RE\ (\%) = \frac{1}{tot} \sum_{v=1}^{tot} \frac{(PET_{pred})_v - (PET_{ref})_v}{(PET_{ref})_v} \times 100\% \quad (6)$$

- **Root Mean Squared Error (RMSE):** Measures the average of the squared differences between the predicted and reference values. It is useful for quantifying the deviation in predictions from the observed values across the dataset.

$$RMSE = \sqrt{\frac{1}{tot}\sum_{v=1}^{tot}((PET_{pred})_v - (PET_{ref})_v)^2} \quad (7)$$

Where tot refers to the total number of voxels, and PET_{pred} and PET_{ref} indicate the predicted image via DL model and the ground truth image, respectively.

- **Peak Signal-to-Noise Ratio (PSNR):** Evaluates the ratio of the maximum possible signal to the corrupting noise.

$$\mathrm{PSNR(dB)} = 10\log_{10}\left(\frac{\mathrm{Peak}^2}{\mathrm{MSE}}\right) \quad (8)$$

In Eq. 8, Peak represents the maximum intensity value in the image.

- **Structural Similarity Index (SSIM):** Assesses the perceptual quality of the predicted images relative to the reference images.

$$SSIM(PET_{pred}, PET_{ref}) = \frac{(2\mu_{pred}\mu_{ref} + c_1)(2\sigma_{pred,ref} + c_2)}{(\mu_{pred}^2 + \mu_{ref}^2 + c_1)(\sigma_{pred}^2 + \sigma_{ref}^2 + c_2)} \quad (9)$$

where: μ_{pred} and μ_{ref} are the averages of the pixel intensities in the predicted PET images (PET_{pred}) and the CT-attenuation corrected PET images (PET_{ref}), respectively. σ_{pred}^2 and σ_{ref}^2 are the variances of the pixel intensities in the predicted and CT-attenuation corrected PET images, respectively. $\sigma_{pred,ref}$ is the covariance of the predicted and CT-attenuation corrected PET images. $c_1 = (k_1 L)^2$ and $c_2 = (k_2 L)^2$ are constants to stabilize the division with a weak denominator; L is the dynamic range of the pixel values (typically $2^{bit\ per\ pixel} - 1$). k_1= 0.01 and k_2=0.03 is the default value for the stabilization constants.

Results

Quantitative assessment

Cross-Center Results:

This section evaluated the two proposed DL algorithms on the 68Ga-PET dataset (IMCM and ADCM). We tested the trained DL model with two internal and external test sets to evaluate its robustness. The internal test sets included 8 subjects from 4 different centers as an external test set and 12 subjects from an external, non-seen center. Figure 6 displays the quantitative accuracy of the deep learning-based images compared to the ground-truth MAC images for internal and external centers. The results demonstrate that both DL methods effectively performed some degree of attenuation and scattering correction across these centers. Refer to the Supplementary Material in Figure 1 for a detailed center-wise analysis.

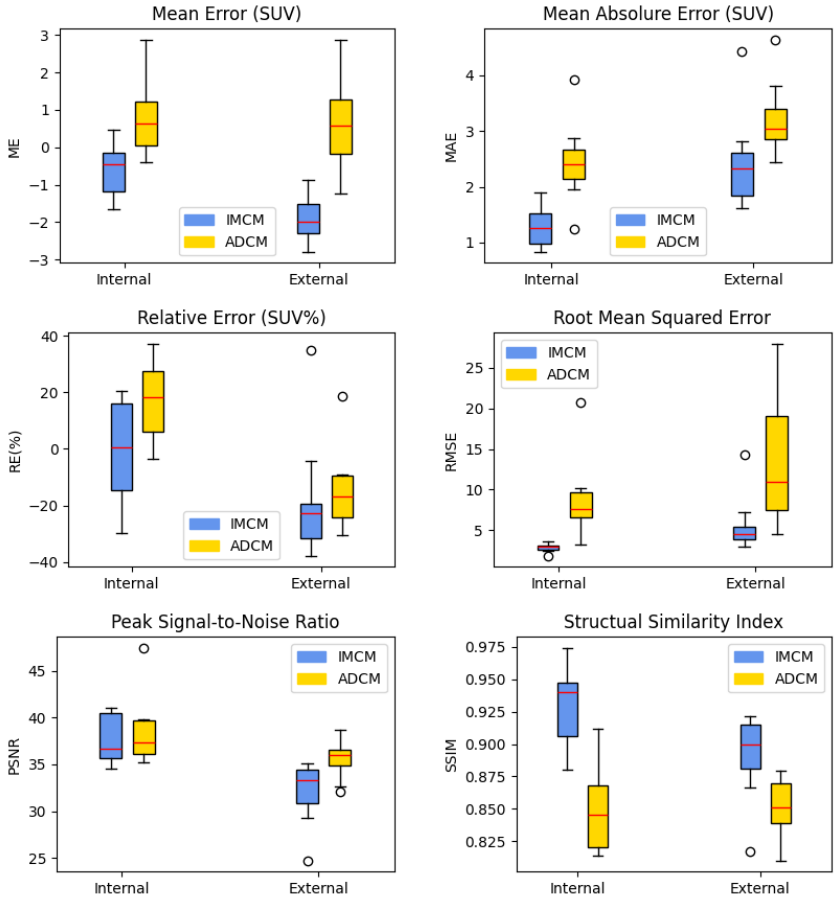

Figure 9: Quantitative metrics for the IMCM and ADCM methods across internal and external centers, including mean error (SUV), mean absolute error (SUV), relative error (SUV%), root mean squared error, peak signal-to-noise ratio, and structural similarity index.

For the external center, ADCM yielded a ME of -0.63±0.96 (CI 95%: -1.23 to -0.03), an MAE of 3.072±1.01 (CI 95%: 2.81 to 3.33), and a RE of -8.14±27.36% (CI 95%: -21.76 to 5.48). In contrast, the IMCM demonstrated improved consistency with an ME of -1.83±1.39 (CI 95%: -2.80 to -0.87) and an MAE of 2.59±0.93 (CI 95%: 2.39 to 2.79). Internal centers showed ADCM produced an ME of 0.37±1.45 (CI 95%: -0.55 to 1.30) and an MAE of 2.34±0.77 (CI 95%: 2.19 to 2.49). IMCM showed a lower ME of -0.36±0.84 (CI 95%: -0.76 to 0.03) and an MAE of 1.41±0.33 (CI 95%: 1.36 to 1.47). PSNR also favored the IMCM method, with 35.53±2.12 (CI 95%: 34.9 to 36.2) compared to 38.25±1.92

(CI 95%: 37.6 to 38.9) for the ADCM method. Notably, SSIM was superior for IMCM in the external center, at 0.88±0.020 (CI 95%: 0.87 to 0.89). Details are available in the Supplementary Material, table 1.

In addition to voxel-wise assessments, model performance was further validated through various statistical tests, which compared image-derived metrics between different training models. The Wilcoxon test was used due to the data's non-normal distribution, as evidenced by the Shapiro-Wilk tests. The Wilcoxon test showed that the ADCM and IMCM datasets were significantly different for all metrics except RE (SUV%), where the p-value does not indicate a statistically significant difference threshold of 0.05. IMCM consistently shows lower errors, a higher PSNR, and higher SSIM values, indicating superior image quality and more reliable estimations. These findings are further detailed in Supplementary Material 2, Statistical test.

In the analysis of the joint histograms, the voxel-wise correlation across the different centers for both methods was visualized in Figure 11. A clear difference in predictive accuracy and linearity in SUV estimation was demonstrated. In the external center, the IMCM regression slope of 0.65 ± 0.02 with an R-value of 0.949 clearly showed a systematic underestimation over the range of predicted SUV values, compared to ADCM, which showed a slope of 1.18 ± 0.10 and an R^2 of 0.850, suggesting a trend towards overestimation potentially linked to very high SUV values that might not be clinically advantageous.

In internal centers, the behavior of the methods differed, with the IMCM method being closer to the ideal prediction, especially evident at center C3 with a regression slope of 0.87 ± 0.01 and an R^2 of 0.988. On the other hand, the ADCM method had slopes greater than one in some cases (1.13 ± 0.03 at C2 and 1.19 ± 0.03 at C4).

The voxel-wise analysis further confirmed these findings, showing larger discrepancies in centers where ADCM predicted significantly higher values. Overall, these results demonstrate that ADCM appears to be closer to the truth in some centers because the R^2-values are higher. However, the reliability and clinical usefulness of ADCM can be called into question. IMCM demonstrated image quality comparable to MAC and preserved more detailed information with lower noise compared to ADCM.

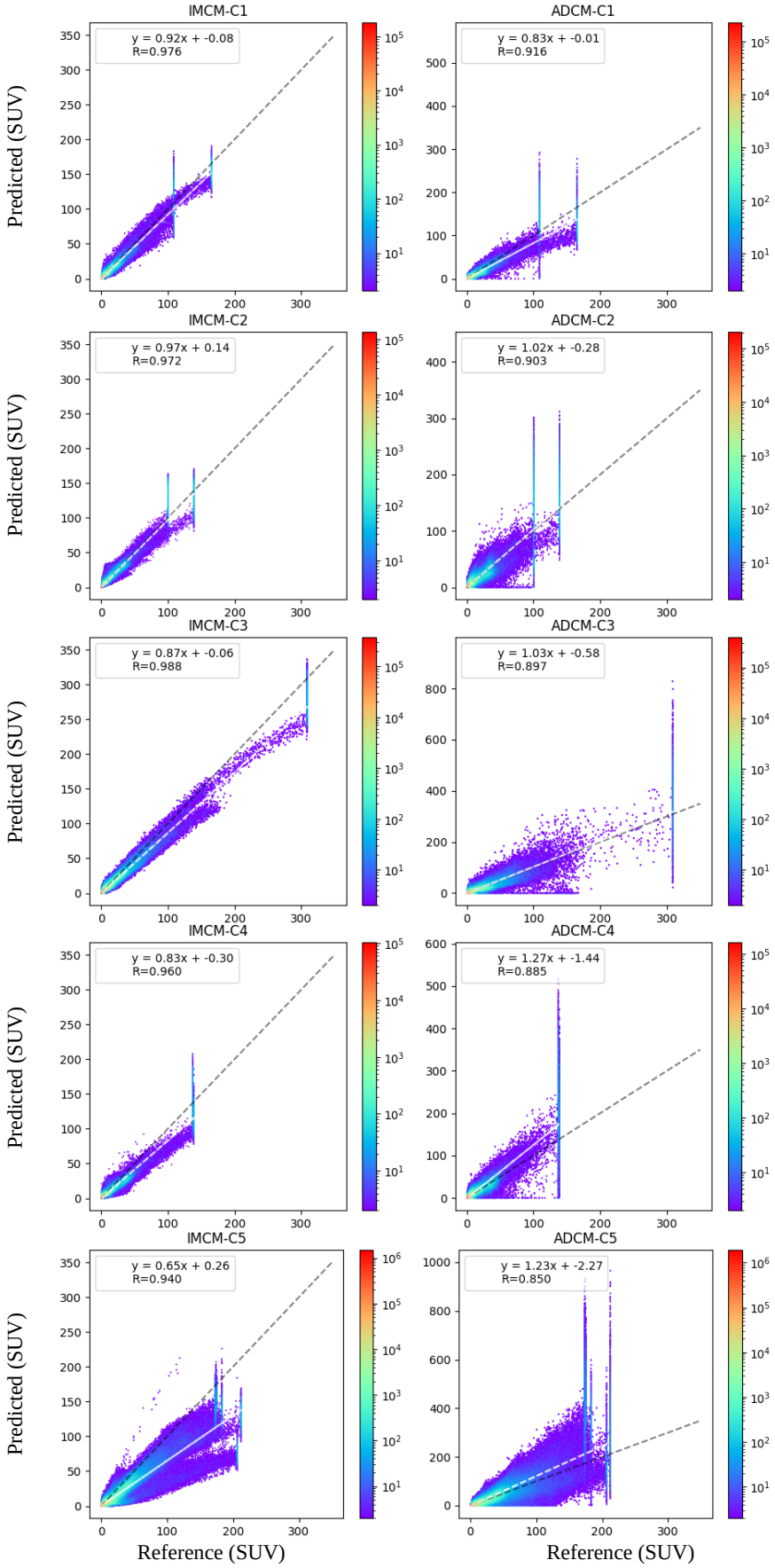

Figure 10: Joint histogram analysis displaying the correlation between activity concentration in DL-IMCM and DL-ADCM images versus reference MAC images serving as the ground truth. Note that a logarithmic scale was used to display the SUV levels. C1-4 are internal centers, while C5 is an external center.

Cross-Tracer Results:

As part of our assessment of generalization capabilities across different tracer types, IMCM was initially tested without specific tuning for cross-tracer variations. As proved before, the results revealed that the IMCM, without prior tuning, struggled to maintain its efficacy when applied to different radiopharmaceutical tracers (66). In this respect, this outcome contrasts with the ADCM's claim, which asserts this approach can handle differences between tracers and anatomical structures without any tuning adjustments. As a part of the generalization assessment among different tracer forms, IMCM was first tested without specific tuning for cross-tracer variation. As mentioned before, the results show the IMCM model, without prior tuning, struggled to maintain its performance when applied to different radiopharmaceutical tracers (39).

So, the ^{18}F-FDG-PET dataset was used as a cross-tracer in this study to test the two proposed DL algorithms: TL-MC (the tuned version of IMCM) and ADCM. We tested the trained DL model to evaluate its robustness, which included 20 subjects from 2 different centers as external non-seen centers. Figure 12 showcases a sample coronal slice of IMCM, TL-MC, and ADCM on cross-tracer subjects. The significant drop in accuracy and increased error rates highlight the challenges in achieving robust cross-tracer generalization with a single, unified model approach. These results show how important it is to tune the model specifically to each tracer's specific properties. This will make the model more useful and accurate in various clinical settings.

The two approaches, TL-MC and ADCM, indicate significant differences in error metrics. Both ME and MAE indicated much smaller error margins for the TL-MC, with the overall mean values reflecting better accuracy than the ADCM. The TL-MC ME deviated narrowly by -0.10±0.76, while the ADCM deviated by 0.82±0.70, signifying a much wider spread of the SUV estimates (Figure 13). These are shown as RE%. This also confirms that TL-MC had a better performance. The RE spread was relatively lower for TL-MC, averaging at 30±50%, in contrast with ADCM, where the spread was much broader at 50±100%.

TL-MC gave a lower RMSE of 2.0 ± 0.6, which pointed out consistency and reliability compared to ADCM's 3.2 ± 1.1. It was also better than ADCM in image quality metrics, with higher PSNR and SSIM values, showing tighter control over noise and structural fidelity.

Altogether, these findings point towards superiority in the use of TL-MC over ADCM in terms of accuracy and consistency in all major key PET imaging metrics, and the use of this approach is recommended in clinical practice where precision is critical. The data makes a compelling case that TL-MC should be preferred with respect to its strong performance in consistently keeping lower errors in the images. For a comprehensive view and deeper analysis, refer to the box plots in Figure 9. Detailed statistical comparisons of these metrics are illustrated in Supplementary Material 2, Tables 3 and 4, provided.

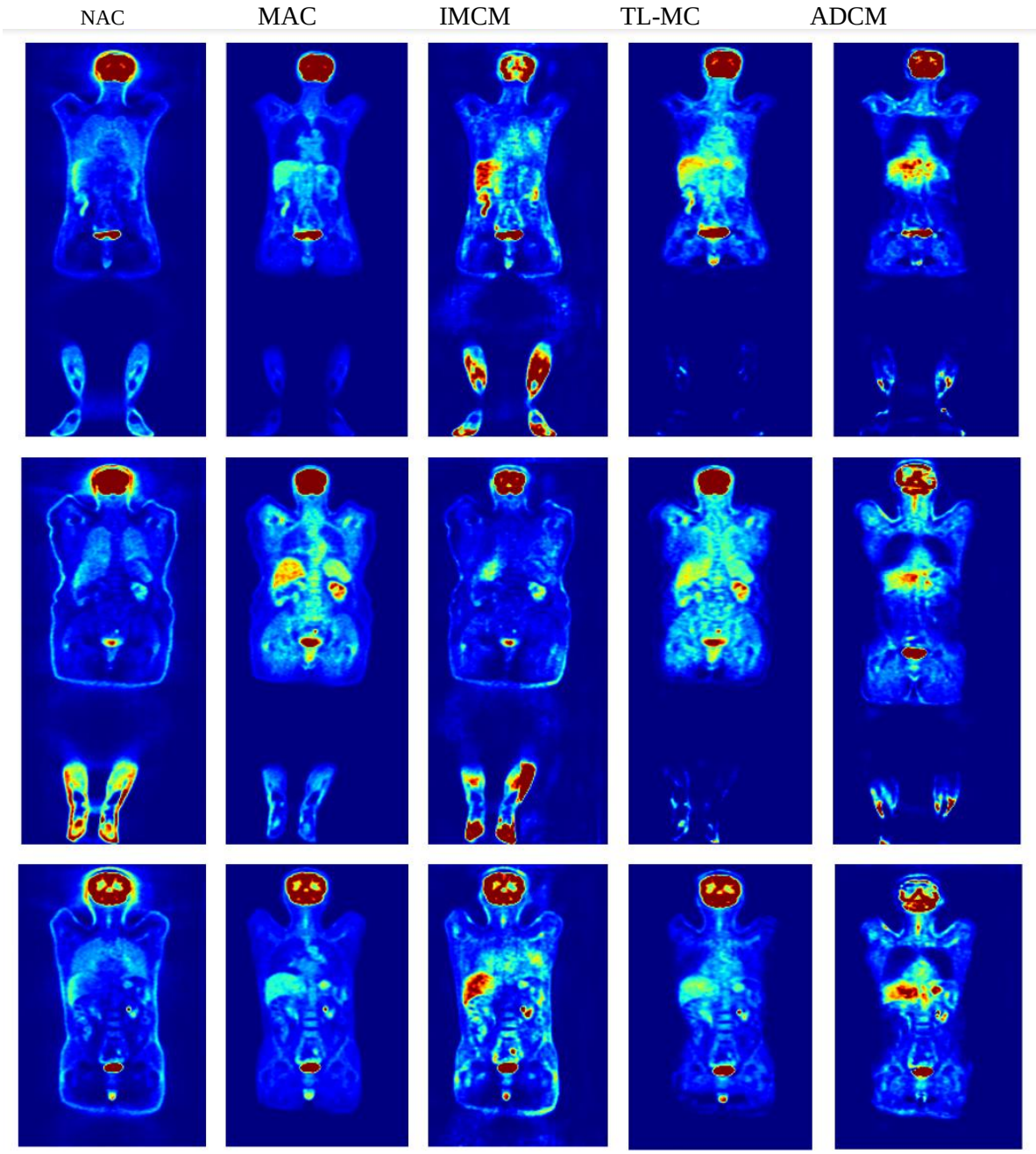

Figure 11: From left to right, a coronal slice of NAC, MAC, IMCM, TL-MC, and ADCM on cross-tracer subjects, respectively.

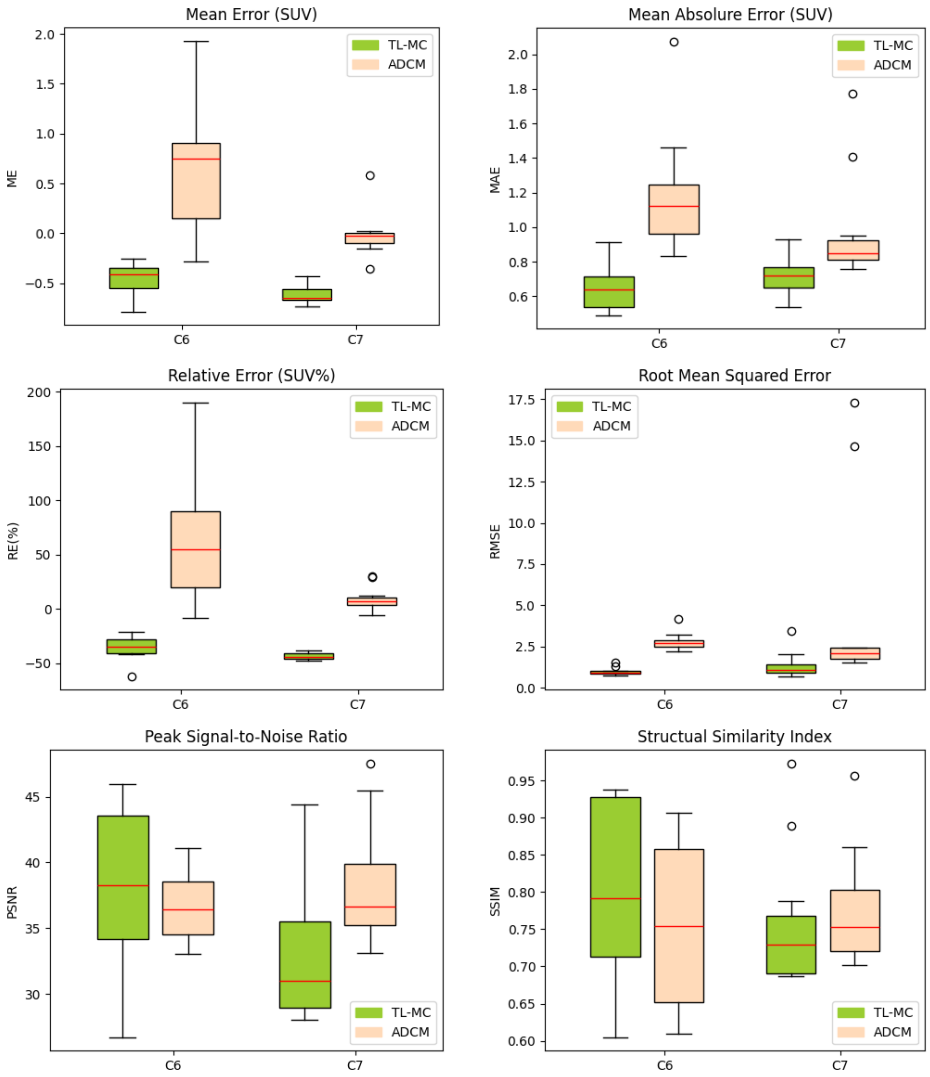

Figure 12: Comparative Analysis of Imaging Metrics Between ADCM and IMCM Methods. The box plots depict the distribution of mean error (SUV), mean absolute error (SUV), relative error (SUV%), root mean squared error, peak signal-to-noise ratio, and structural similarity index across centers C6 and C7.

Further investigation through joint histogram analysis of the TL-MC and ADCM models is different centers provides precise understanding of each model's predictive capabilities for SUVs. The TL-MC model closely matches to reference values, as evidenced by regression slopes of 0.98 ± 0.38 and 0.69 ± 0.08 at two respective centers. Notably, this model also has high correlation coefficients of 0.915 and 0.918, emphasizing its precision in SUV prediction, despite a tendency to slightly underestimate values, particularly at Center C7 as presented in the analysis.

On the other hand, the ADCM model has lower correlation coefficients of 0.660 and 0.678, even though its regression slopes are higher at 1.10 ± 0.46 and 1.35 ± 0.66, which means it overestimates the data. This discrepancy highlights the lesser consistency and reliability of its predictions when compared to TL-MC. Contrary to intuitive expectations of better correlation, the higher slopes observed in ADCM indicate a greater deviation from the reference line, pointing to a systematic error in overestimating SUVs.

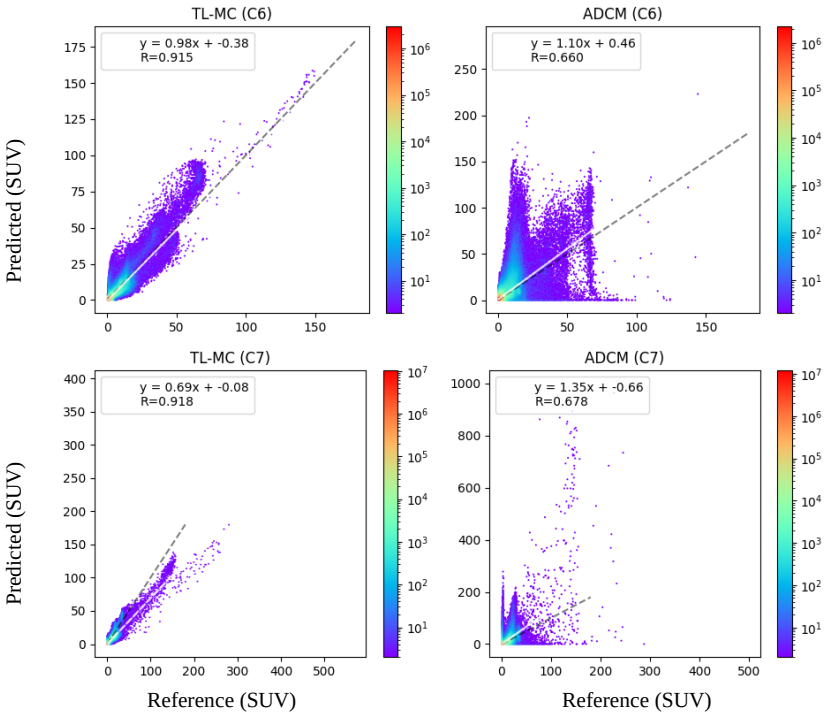

Figure 13: Joint histogram analysis displaying the correlation between activity concentration in TL-MC and ADCM images versus reference MAC images serving as the ground truth for cross-tracer. Note that a logarithmic scale was used to display the SUV levels.

Case Study on Artifact Images

This section examined a series of case studies involving repeated scans. These repeated scans have been requested by nuclear medicine physicians shortly after initial assessments. Figures 15, 16, and 17 display the imaging results for patients with halo artifacts in the pelvic, kidney, diaphragm, lung, liver, and spleen regions. These artifacts were removed in the repeated scan. The ICMC method produced artifact-free images of high quality, diagnostic confidence, and nearly identical to the initial scan. Figure 18 features patients with a halo artifact in the kidneys. A repeated scan was conducted in this region due to the initial scan's low image quality and diagnostic confidence. Unfortunately, in some cases, the repeated scan could not remove these artifacts. Nonetheless, the ICMC model successfully eliminated the artifact in both the original and subsequent scans.

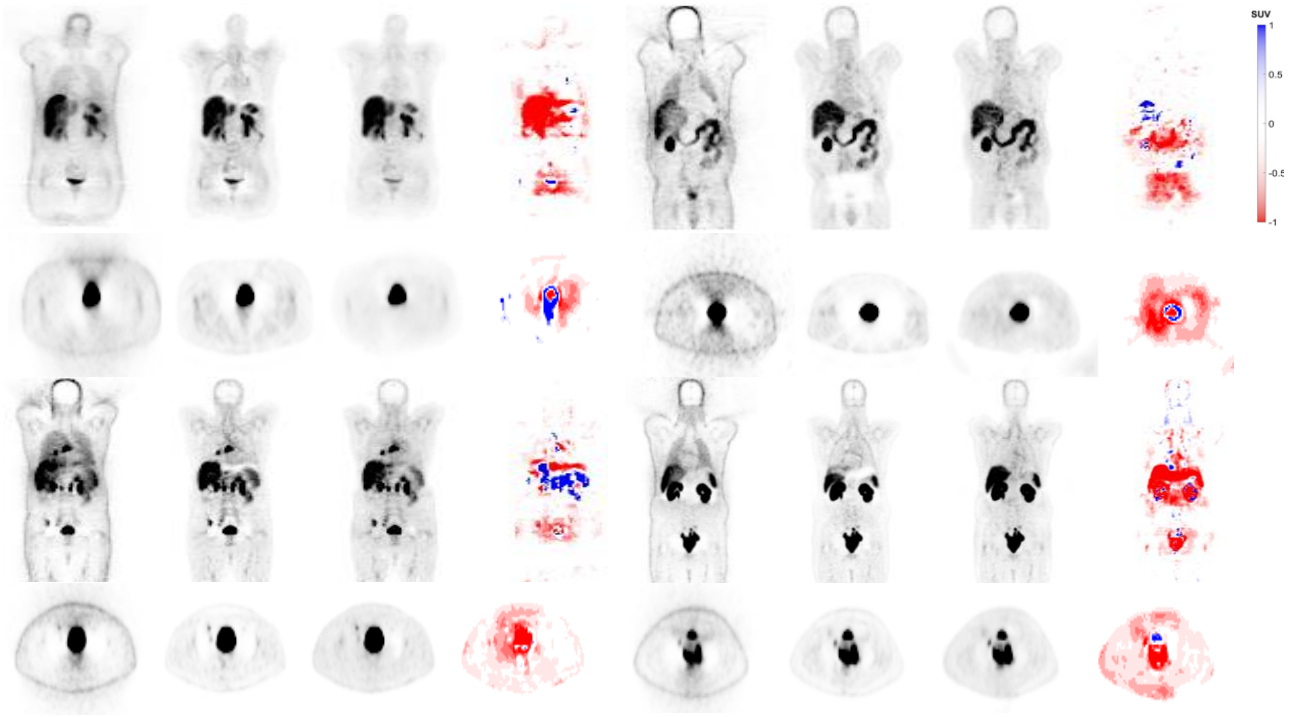

Figure 14: Coronal and axial views of 12 clinical studies showing from left to right NAC, MAC, IMCM-DL and the difference images of MAC and DL image. The images generated using the IMCM approach successfully corrected the halo artefact in pelvic area.

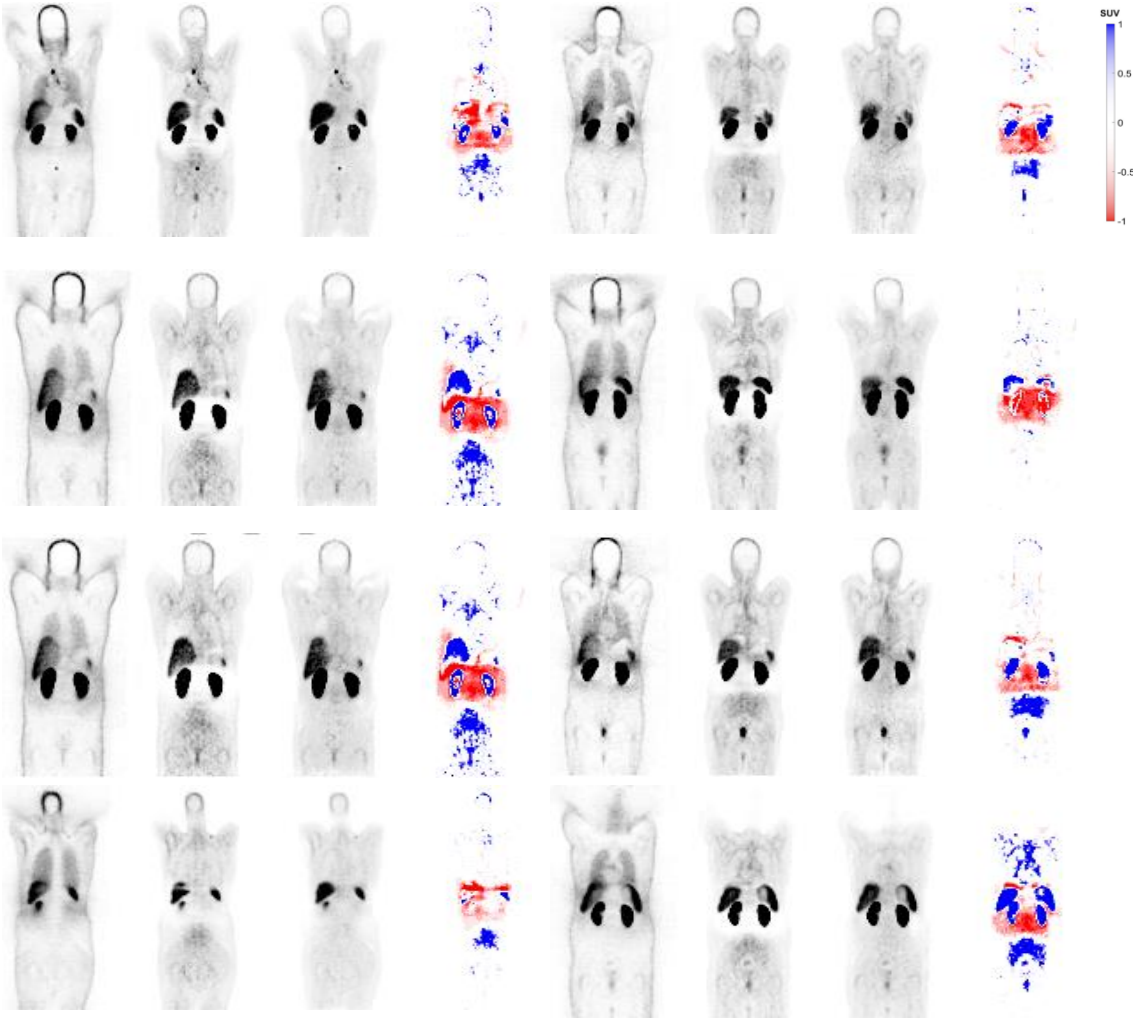

Figure 15: Coronal views of 8 clinical studies, representing from left to right: NAC, MAC, IMCM-DL and the difference images of MAC and DL image. Our method effectively disentangles halo artefacts in the kidney area.

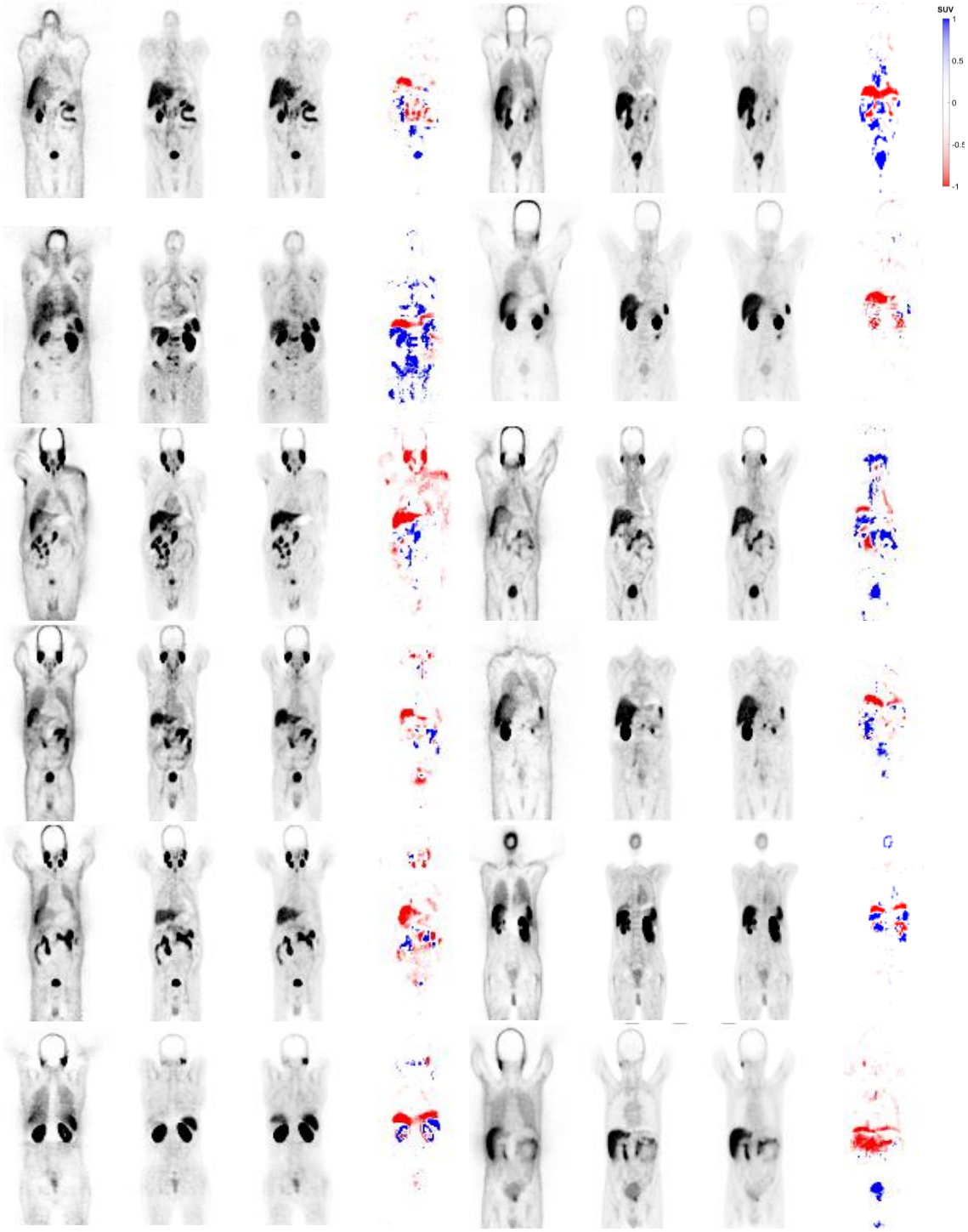

Figure 16: Coronal views of 12 clinical studies showing from left to right NAC, MAC, IMCM-DL, and the difference images of MAC and DL image. The images generated using the IMCM approach successfully corrected the mismatch artifact in the diaphragm, lung, liver, and spleen regions.

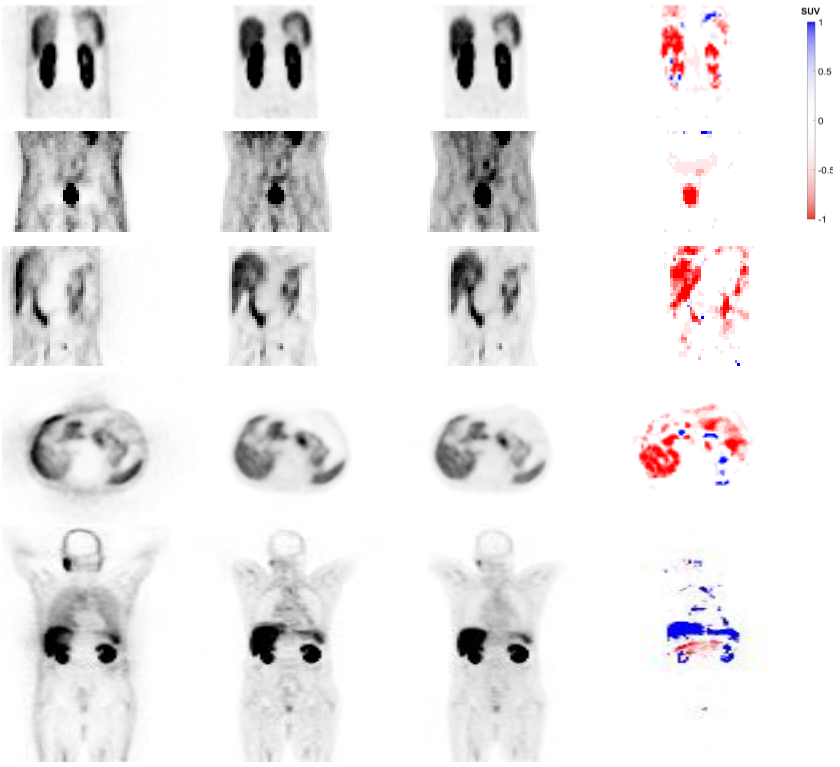

Figure 17: Coronal and axial views showing from left to right NAC, MAC, IMCM-DL and the difference images of MAC and DL image. The repeated scan which was requested right after the initial scan. The IMCM image recovered high quality and high diagnostic confidence for both scans.

Discussion

Various deep learning-based attenuation scatter correction (DL-ASC) methods have been developed for PET imaging (21,42,44,67,70,71,73,74). These include indirect approaches that generate attenuation maps from MRI or CT images. For instance, studies have employed GANs to achieve pseudo-CT images from NAC PET scans in both brain and whole-body PET imaging (40,41,66,73,75,76). Furthermore, the MLAA algorithm has been improved by incorporating deep learning to mitigate common issues such as crosstalk artifacts, slow convergence, and noisy attenuation maps (33,77,78). Direct DL-ASC methods bypass traditional methods by making ASC PET images directly from NAC images. This was first used in brain PET imaging and then tested in ^{18}F-FDG PET studies (41).

A significant challenge arises with the low tracer activity and the extensive positron range of ^{68}Ga-labelled pharmaceuticals, which generally produce lower-quality images compared to ^{18}F-labelled compounds. Initially, employing DL for direct ASC in PET might seem overly reliant on advanced technology (18,25,79,80). However, our findings indicate that it enhances both quantitative and qualitative aspects of PET images and effectively identifies and corrects mismatches and halo artifacts without needing anatomical images. While indirect techniques require reconstructions to produce ASC PET images, they often fail to address halo artifacts that arise during the reconstruction phase and are predominantly influenced by the PET images themselves.

This study has demonstrated that a single universal model may not be effective due to variations in tracer-injected activity across different hospitals. There is a need to tune radiotracer-wise models using heterogeneous datasets to address these discrepancies. However, using large and heterogeneous datasets from different hospitals in the same tracer can compensate for the differences in equipment, image acquisition, and reconstruction strategies. In our research, we utilized different data from various hospitals, which enhanced the accuracy of ASC in PET images when implementing a shared model across different hospitals for identical radiotracer imaging.

Furthermore, we employed the IMCM for additional qualitative analysis. Through quantitative assessments, we observed the substantial impact that radiotracers and scanners have on model performance. Notably, IMCM greatly increased the quantitative accuracy across various scanners, indicating the need for model tuning using transfer learning that is tailored to specific tracer situations and thus performs better than ADCM. IMCM showed enhanced efficiency when different scanners utilized the same radiotracer, compared to when various radiotracers were employed on the same scanner. We also found that the source of the data, including the type of scanner and radiotracer used, significantly affected ADCM's effectiveness, contrary to initial assumptions.

While the ADCM method focuses on decomposing the PET image correction process into separating anatomical and radiotracer-dependent information, our investigation couldn’t prove that it may not be able to handle the differences between variant scanners and radiotracers well. This underscores the need for more robust, adaptable models like IMCM, which not only accommodate but thrive on the heterogeneity inherent in multi-center clinical data.

The joint histogram analysis raised questions regarding the calibration and reliability of the ADCM method in clinical situations. Notably, the overestimations observed by ADCM, especially in cross-center measurements, could lead to incorrect diagnoses in conditions where the accuracy of the SUV estimation is critical. The systematic bias towards higher SUV values, while giving a superficial appearance of accuracy as a higher R^2, suggests underlying problems in the algorithm or its application across different PET systems.

In contrast, the IMCM method’s outcome with lower regression slopes, higher correlation coefficients, and more reliable SUV estimations, particularly in internal centers, highlights its application in the clinic. The variance between IMCM and ADCM’s performance shows the necessity for rigorous validation of imaging algorithms to ensure uniform performance across different settings. The analysis

across cross-tracer highlights the critical aspect that a higher slope does not necessarily equate to better correlation. Instead, the consistency with which predictions align with actual values, as measured by correlation coefficients, provides a more substantial indication of a model's effectiveness. Despite lower regression slopes, the TL-MC model demonstrates a more reliable and consistent performance in capturing the true behavior of SUVs across the studied centers. CT-ASCs are a primary adjustment for quantitative ^{68}Ga PET imaging. However, this process can introduce mismatches and halo artifacts in ^{68}Ga PET images, potentially altering patient diagnosis and prognosis. These artifacts are challenging to detect and correct in real clinical settings. Our developed model does not require image reconstruction with ASC. The qualitative analysis demonstrated the effectiveness of our proposed model in detecting and removing mismatches and halo artifacts in the chest, abdomen, and pelvic regions without needing ground truth in ^{68}Ga PET images. We also observed scenarios where repeated scans, typically conducted to eliminate artifacts, failed and even exacerbated them. Here, our DL algorithms could distinguish and correct these issues independently of the ground truth.

Previous studies' predominant limitation lies in their single-center datasets, which restrict the generalizability of DL models (17,70,71). Our current study employs a multi-center approach to address this issue. Future research should explore clinical imaging parameters such as SUV_{mean}, SUV_{max}, and total lesion metabolism, providing a more comprehensive analysis of the IMCM model's performance. These metrics, along with an assessment of the most relevant radiomic features within the sphere of influence, will provide crucial insights into the model's effectiveness under various clinical conditions.

Future investigations should focus on the performance of the IMCM model in organ-specific evaluations for both clean and artifactual images. Such targeted analysis would provide a more specific understanding of the model's capabilities in different clinical situations. In addition, rigorous statistical testing of categorized outcomes will be important. These tests will provide deeper insights into the model's consistency and reliability across different diagnostic categories and will help refine the model's application and improve diagnostic accuracy in practical healthcare settings.

Conclusion

In this thesis, we have demonstrated the efficacy of an Integrated multi-center Dynamic Unet deep learning framework for artifact detection and correction in PET imaging of ^{68}Ga-labelled compounds. The approach leverages large datasets from multiple centers. Through the incorporation of transfer learning concepts, we have developed site-specific models that significantly outperform centralized models and those based on single-center data, thereby addressing a major limitation in the field of medical imaging. Our model effectively detected and corrected artifacts. This enhancement is vital for making therapeutic decisions in the field of oncology, where PET imaging plays a central role in diagnosing, planning treatments, and evaluating responses. By using Dyn-Unet architecture and other advanced deep learning techniques, our method has not only improved image quality but also greatly decreased the appearance of common artifacts like halo and mismatch artifacts, especially in ^{68}Ga-PET imaging. The effective implementation of our models in different centers highlights their resilience and flexibility, which are essential for general acceptance in clinical settings.

References

1. Cerqueira MD. Cardiac SPECT or PET?: Is there still a debate? Vol. 29, Journal of Nuclear Cardiology. 2022.

2. Sarikaya I. Cardiac applications of PET. Nucl Med Commun [Internet]. 2015 Oct;36(10):971–85. Available from: https://journals.lww.com/00006231-201510000-00002

3. Catana C, Procissi D, Wu Y, Judenhofer MS, Qi J, Pichler BJ, et al. Simultaneous in vivo positron emission tomography and magnetic resonance imaging. Proc Natl Acad Sci U S A. 2008;105(10).

4. Boellaard R, Delgado-Bolton R, Oyen WJG, Giammarile F, Tatsch K, Eschner W, et al. FDG PET/CT: EANM procedure guidelines for tumour imaging: version 2.0. Vol. 42, European Journal of Nuclear Medicine and Molecular Imaging. 2015.

5. Karakatsanis NA, Fokou E, Tsoumpas C. Dosage optimization in positron emission tomography: state-of-the-art methods and future prospects. Am J Nucl Med Mol Imaging. 2015;5(5).

6. Fahey FH, Treves ST, Adelstein SJ. Minimizing and communicating radiation risk in pediatric nuclear medicine. J Nucl Med Technol. 2012;40(1).

7. Zaidi H, MML. Scatter Compensation Techniques in PET. PET clinics. PET Clin [Internet]. 2007 [cited 2023 Nov 20];2(2):219–34. Available from: https://doi.org/10.1016/j.cpet.2007.10.003

8. Baer M, Kachelrie M. Hybrid scatter correction for CT imaging. Phys Med Biol. 2012;57(21).

9. Watson CC, Casey ME, Michel C, Bendriem B. Advances in scatter correction for 3D PET/CT. In: IEEE Nuclear Science Symposium Conference Record. 2004.

10. Zaidi H, Koral KF. Scatter modelling and compensation in emission tomography. Vol. 31, European Journal of Nuclear Medicine and Molecular Imaging. 2004.

11. Pettinato C, Nanni C, Farsad M, Castellucci P, Sarnelli A, Civollani S, et al. Artefacts of PET/CT images. Biomed Imaging Interv J. 2006;2(4).

12. Lammertsma AA. Forward to the past: The case for quantitative PET imaging. Vol. 58, Journal of Nuclear Medicine. 2017.

13. Presotto L, Busnardo E, Perani D, Gianolli L, Gilardi MC, Bettinardi V. Simultaneous reconstruction of attenuation and activity in cardiac PET can remove CT misalignment artifacts. Journal of Nuclear Cardiology. 2016;23(5).

14. Mostafapour S, Greuter M, van Snick JH, Brouwers AH, Dierckx RAJO, van Sluis J, et al. Ultra-low dose CT scanning for PET/CT. Med Phys. 2024;51(1).

15. Sureshbabu W, Mawlawi O. PET/CT Imaging Artifacts* [Internet]. Vol. 33, J Nucl Med Technol. 2005. Available from: http://www.snm.org/ce_online

16. Mawlawi O, Pan T, Macapinlac HA. PET/CT Imaging Techniques, Considerations, and Artifacts. J Thorac Imaging [Internet]. 2006;21(2). Available from: https://journals.lww.com/thoracicimaging/fulltext/2006/05000/pet_ct_imaging_techniques,_considerations,_and.2.aspx

17. Shiri I, Salimi Y, Maghsudi M, Jenabi E, Harsini S, Razeghi B, et al. Differential privacy preserved federated transfer learning for multi-institutional 68Ga-PET image artefact detection and disentanglement. Eur J Nucl Med Mol Imaging. 2023;

18. Shiri I, Salimi Y, Hervier E, Pezzoni A, Sanaat A, Mostafaei S, et al. Artificial Intelligence-Driven Single-Shot PET Image Artifact Detection and Disentanglement: Toward Routine Clinical Image Quality Assurance. Clin Nucl Med. 2023 Dec 1;48(12):1035–46.

19. Abdoli M, Dierckx RAJO, Zaidi H. Metal artifact reduction strategies for improved attenuation correction in hybrid PET/CT imaging. Vol. 39, Medical Physics. 2012.

20. Ghafarian P, Aghamiri SMR, Ay MR, Rahmim A, Schindler TH, Ratib O, et al. Is metal artefact reduction mandatory in cardiac PET/CT imaging in the presence of pacemaker and implantable cardioverter defibrillator leads? Eur J Nucl Med Mol Imaging. 2011;38(2).

21. Lindemann ME, Nensa F, Quick HH. Impact of improved attenuation correction on 18F-FDG PET/MR hybrid imaging of the heart. PLoS One. 2019;14(3).

22. McQuaid SJ, Hutton BF. Sources of attenuation-correction artefacts in cardiac PET/CT and SPECT/CT. Eur J Nucl Med Mol Imaging. 2008;35(6).

23. Magota K, Numata N, Shinyama D, Katahata J, Munakata Y, Maniawski PJ, et al. Halo artifacts of indwelling urinary catheter by inaccurate scatter correction in 18F-FDG PET/CT imaging: incidence, mechanism, and solutions. EJNMMI Phys. 2020;7(1).

24. Heußer T, Mann P, Rank CM, Schäfer M, Dimitrakopoulou-Strauss A, Schlemmer HP, et al. Investigation of the halo-artifact in 68Ga-PSMA-11-PET/MRI. PLoS One. 2017;12(8).

25. Afshar-Oromieh A, Wolf M, Haberkorn U, Kachelrieß M, Gnirs R, Kopka K, et al. Effects of arm truncation on the appearance of the halo artifact in 68Ga-PSMA-11 (HBED-CC) PET/MRI. Eur J Nucl Med Mol Imaging. 2017;44(10).

26. Sarikaya I, Sarikaya A. PET/CT Image Artifacts Caused by the Arms. J Nucl Med Technol. 2021;49(1).

27. Lodge MA, Mhlanga JC, Cho SY, Wahl RL. Effect of patient arm motion in whole-body PET/CT. Journal of Nuclear Medicine. 2011;52(12).

28. Dinges J, Nekolla SG, Bundschuh RA. Motion artifacts in oncological and cardiac PET imaging. Vol. 8, PET Clinics. 2013.

29. Presotto L. The long fight against motion artifacts in cardiac PET. Vol. 29, Journal of Nuclear Cardiology. 2022.

30. Piccinelli M, Votaw JR, Garcia E V. Motion Correction and Its Impact on Absolute Myocardial Blood Flow Measures with PET. Vol. 20, Current Cardiology Reports. 2018.

31. Chun SY, Kim KY, Lee JS, Fessier JA. Joint estimation of activity distribution and attenuation map for TOF-PET using alternating direction method of multiplier. In: Proceedings - International Symposium on Biomedical Imaging. 2016.

32. Mehranian A, Arabi H, Zaidi H. Vision 20/20: Magnetic resonance imaging-guided attenuation correction in PET/MRI: Challenges, solutions, and opportunities. Med Phys. 2016;43(3).

33. Li S, Wang G. Modified kernel MLAA using autoencoder for PET-enabled dual-energy CT. Philosophical Transactions of the Royal Society A: Mathematical, Physical and Engineering Sciences. 2021;379(2204).

34. Akbarzadeh A, Ay MR, Ahmadian A, Riahi Alam N, Zaidi H. MRI-guided attenuation correction in whole-body PET/MR: Assessment of the effect of bone attenuation. Ann Nucl Med. 2013;27(2).

35. Carney JPJ, Townsend DW, Rappoport V, Bendriem B. Method for transforming CT images for attenuation correction in PET/CT imaging. Med Phys. 2006;33(4).

36. Kinahan PE, Townsend DW, Beyer T, Sashin D. Attenuation correction for a combined 3D PET/CT scanner. Med Phys. 1998;25(10).

37. Alessio AM, Kohlmyer S, Branch K, Chen G, Caldwell J, Kinahan P. Cine CT for attenuation correction in cardiac PET/CT. Journal of Nuclear Medicine. 2007;48(5).

38. Alberts I, Hünermund JN, Prenosil G, Mingels C, Bohn KP, Viscione M, et al. Clinical performance of long axial field of view PET/CT: a head-to-head intra-individual comparison of the Biograph Vision Quadra with the Biograph Vision PET/CT. Eur J Nucl Med Mol Imaging. 2021;48(8).

39. Guo R, Xue S, Hu J, Sari H, Mingels C, Zeimpekis K, et al. Using domain knowledge for robust and generalizable deep learning-based CT-free PET attenuation and scatter correction. Nat Commun. 2022 Dec 1;13(1).

40. Yang J, Sohn JH, Behr SC, Gullberg GT, Seo Y. Ct-less direct correction of attenuation and scatter in the image space using deep learning for whole-body fdg pet: Potential benefits and pitfalls. Radiol Artif Intell. 2021 Mar 1;3(2).

41. Shiri I, Ghafarian P, Geramifar P, Leung KHY, Ghelichoghli M, Oveisi M, et al. Direct attenuation correction of brain PET images using only emission data via a deep convolutional encoder-decoder (Deep-DAC). Eur Radiol. 2019 Dec 1;29(12):6867–79.

42. Lee JS. A Review of Deep-Learning-Based Approaches for Attenuation Correction in Positron Emission Tomography. Vol. 5, IEEE Transactions on Radiation and Plasma Medical Sciences. 2021.

43. Qian H, Rui X, Ahn S. Deep Learning Models for PET Scatter Estimations. In: 2017 IEEE Nuclear Science Symposium and Medical Imaging Conference (NSS/MIC). 2017. p. 1–5.

44. Liu F, Jang H, Kijowski R, Zhao G, Bradshaw T, McMillan AB. A deep learning approach for18 f-fdg pet attenuation correction. EJNMMI Phys. 2018;5(1).

45. Wu X, Sahoo D, Hoi SCH. Recent advances in deep learning for object detection. Neurocomputing. 2020;396.

46. Zhao ZQ, Zheng P, Xu ST, Wu X. Object Detection with Deep Learning: A Review. Vol. 30, IEEE Transactions on Neural Networks and Learning Systems. 2019.

47. Ma X, Wu J, Xue S, Yang J, Zhou C, Sheng QZ, et al. A Comprehensive Survey on Graph Anomaly Detection With Deep Learning. IEEE Trans Knowl Data Eng. 2023;35(12).

48. McLeavy CM, Chunara MH, Gravell RJ, Rauf A, Cushnie A, Staley Talbot C, et al. The future of CT: deep learning reconstruction. Vol. 76, Clinical Radiology. 2021.

49. Ahishakiye E, Van Gijzen MB, Tumwiine J, Wario R, Obungoloch J. A survey on deep learning in medical image reconstruction. Vol. 1, Intelligent Medicine. 2021.

50. Kim SH, Choi YH, Lee JS, Lee SB, Cho YJ, Lee SH, et al. Deep learning reconstruction in pediatric brain MRI: comparison of image quality with conventional T2-weighted MRI. Neuroradiology. 2023;65(1).

51. Jebur RS, Zabil MHBM, Hammood DA, Cheng LK. A comprehensive review of image denoising in deep learning. Multimed Tools Appl. 2023;

52. Tian C, Fei L, Zheng W, Xu Y, Zuo W, Lin CW. Deep learning on image denoising: An overview. Vol. 131, Neural Networks. 2020.

53. Wu H, Liu Y, Wang J. Review of text classification methods on deep learning. Vol. 63, Computers, Materials and Continua. 2020.

54. Ibrahim DM, Elshennawy NM, Sarhan AM. Deep-chest: Multi-classification deep learning model for diagnosing COVID-19, pneumonia, and lung cancer chest diseases. Comput Biol Med. 2021;132.

55. Krishna MM, Neelima M, Harshali M, Rao MVG. Image classification using Deep learning. International Journal of Engineering and Technology(UAE). 2018;7.

56. Liu X, Song L, Liu S, Zhang Y. A review of deep-learning-based medical image segmentation methods. Sustainability (Switzerland). 2021;13(3).

57. Wang R, Lei T, Cui R, Zhang B, Meng H, Nandi AK. Medical image segmentation using deep learning: A survey. IET Image Process. 2022;16(5).

58. Minaee S, Boykov Y, Porikli F, Plaza A, Kehtarnavaz N, Terzopoulos D. Image Segmentation Using Deep Learning: A Survey. IEEE Trans Pattern Anal Mach Intell. 2022;44(7).

59. Xia T, Alessio AM, Kinahan PE. Limits of ultra-low dose CT attenuation correction for PET/CT. In: IEEE Nuclear Science Symposium Conference Record. 2009.

60. Prieto E, García-Velloso MJ, Aquerreta JD, Rosales JJ, Bastidas JF, Soriano I, et al. Ultra-low dose whole-body CT for attenuation correction in a dual tracer PET/CT protocol for multiple myeloma. Physica Medica. 2021;84.

61. Wafa B, Moussaoui A. A review on methods to estimate a CT from MRI data in the context of MRI-alone RT. Medical Technologies Journal. 2018;2(1).

62. Lindemann ME, Gratz M, Blumhagen JO, Jakoby B, Quick HH. MR-based truncation correction using an advanced HUGE method to improve attenuation correction in PET/MR imaging of obese patients. Med Phys. 2022;49(2).

63. Sun H, Xi Q, Fan R, Sun J, Xie K, Ni X, et al. Synthesis of pseudo-CT images from pelvic MRI images based on an MD-CycleGAN model for radiotherapy. Phys Med Biol. 2022;67(3).

64. Wang T, Manohar N, Lei Y, Dhabaan A, Shu HK, Liu T, et al. MRI-based treatment planning for brain stereotactic radiosurgery: Dosimetric validation of a learning-based pseudo-CT generation method. Medical Dosimetry. 2019;44(3).

65. Jabbarpour A, Mahdavi SR, Vafaei Sadr A, Esmaili G, Shiri I, Zaidi H. Unsupervised pseudo CT generation using heterogenous multicentric CT/MR images and CycleGAN: Dosimetric assessment for 3D conformal radiotherapy. Comput Biol Med. 2022;143.

66. Shiri I, Arabi H, Geramifar P, Hajianfar G, Ghafarian P, Rahmim A, et al. Deep-JASC: joint attenuation and scatter correction in whole-body 18F-FDG PET using a deep residual network. Eur J Nucl Med Mol Imaging. 2020 Oct 1;47(11):2533–48.

67. Liu F, Jang H, Kijowski R, Bradshaw T, McMillan AB. Deep learning MR imaging-based attenuation correction for PET/MR imaging. Radiology. 2018;286(2).

68. Arabi H, Zaidi H. Deep learning–based metal artefact reduction in PET/CT imaging. Eur Radiol. 2021;31(8).

69. Arabi H, Zaidi H. Truncation compensation and metallic dental implant artefact reduction in PET/MRI attenuation correction using deep learning-based object completion. Phys Med Biol. 2020;65(19).

70. Shiri I, Vafaei Sadr A, Akhavan A, Salimi Y, Sanaat A, Amini M, et al. Decentralized collaborative multi-institutional PET attenuation and scatter correction using federated deep learning. Eur J Nucl Med Mol Imaging. 2023 Mar 1;50(4):1034–50.

71. Shiri I, Sadr A V, Sanaat A, Ferdowsi S, Arabi H, Zaidi H. Federated Learning-based Deep Learning Model for PET Attenuation and Scatter Correction: A Multi-Center Study. In: 2021 IEEE Nuclear Science Symposium and Medical Imaging Conference (NSS/MIC). 2021. p. 1–3.

72. Isensee F, Petersen J, Klein A, Zimmerer D, Jaeger PF, Kohl S, et al. nnU-Net: Self-adapting Framework for U-Net-Based Medical Image Segmentation. In: Informatik aktuell. 2019.

73. Hwang D, Kang SK, Kim KY, Seo S, Paeng JC, Lee DS, et al. Generation of PET attenuation map for whole-body time-of-flight 18F-FDG PET/MRI using a deep neural network trained with simultaneously reconstructed activity and attenuation maps. Journal of Nuclear Medicine. 2019;60(8).

74. McMillan AB, Bradshaw TJ. Artificial Intelligence–Based Data Corrections for Attenuation and Scatter in Position Emission Tomography and Single-Photon Emission Computed Tomography. Vol. 16, PET Clinics. W.B. Saunders; 2021. p. 543–52.

75. Armanious K, Hepp T, Küstner T, Dittmann H, Nikolaou K, La Fougère C, et al. Independent attenuation correction of whole body [18F]FDG-PET using a deep learning approach with Generative Adversarial Networks. EJNMMI Res. 2020;10(1).

76. Izadi S, Shiri I, F. Uribe C, Geramifar P, Zaidi H, Rahmim A, et al. Enhanced direct joint attenuation and scatter correction of whole-body PET images via context-aware deep networks. Z Med Phys. 2024;

77. Shi L, Zhang J, Toyonaga T, Shao D, Onofrey JA, Lu Y. Deep learning-based attenuation map generation with simultaneously reconstructed PET activity and attenuation and low-dose application. Phys Med Biol. 2023;68(3).

78. Hwang D, Kim KY, Kang SK, Seo S, Paeng JC, Lee DS, et al. Improving the accuracy of simultaneously reconstructed activity and attenuation maps using deep learning. Journal of Nuclear Medicine. 2018;59(10).

79. Shiri I, Salimi Y, Sanaat A, Saberi A, Amini M, Akhavanallaf A, et al. Fully Automated PET Image Artifacts Detection and Correction Using Deep Neural Networks Journal of Nuclear Medicine [Internet]. 2022 Jun 1;63(supplement 2):3218. Available from: http://jnm.snmjournals.org/content/63/supplement_2/3218.abstract

80. Shiri I, Sanaat A, Salimi Y, Akhavanallaf A, Arabi H, Rahmim A, et al. PET-QA-Net: Towards Routine PET Image Artifact Detection and Correction using Deep Convolutional Neural Networks. In: 2021 IEEE Nuclear Science Symposium and Medical Imaging Conference (NSS/MIC). 2021. p. 1–3.

Supplementary Material 1

The initial Step from the Segmentation task to the image to image translation

The foundational idea is that if a deep learning model can accurately identify and position organs for segmentation, then it could ostensibly learn to correct an image in the desired style by effectively utilizing the right activation functions, loss functions, and an appropriate architectural design. So, for the first step: Could a model, trained on any images, learn to produce an acceptable output by using the same image as both input and target, focusing initially on visual acceptability rather than quantitative metrics.

We utilized CT images as samples before accessing the original data. The experimental setup involved using these images as both the training inputs and target inputs, aiming to fine-tune the model's hyperparameters to achieve visually satisfactory outputs. This stage was primarily about understanding the influence of various parameters on the initial results and was not concerned with the precision of error metrics.

Fig 1 and Table 1 in this supplementary section illustrate some of the outputs. This stage served an educational purpose, helping us to understand the foundational dynamics of deep learning applications in corrected images.

Table 1: Some specifications of the training approach

crop_size	(512, 512, 32)
transforms	ScaleIntensityRanged(keys=["image", "target"],a_min=-1024, a_max=2048, b_min=0.0, b_max=1.0, clip=**True**), Orientationd(keys=["image", "target"], axcodes="RAS"), Spacingd(keys=["image", "target"], pixdim=(1.5, 1.5, 2.0)), Resized(keys=["image", "target"], spatial_size=crop_size, mode='bilinear'), CenterSpatialCropd(keys=["image", "target"], roi_size=crop_size),
batch_size	4
model	UNet(spatial_dims=3,in_channels=1,out_channels=1,channels=(16, 32, 64),act=(nn.ReLU, {"inplace": **True**}), strides=(2, 2), num_res_units=2, norm=Norm.BATCH)
loss_function	torch.nn.MSELoss()
optimizer	torch.optim.Adam(model.parameters(), 1e-6)

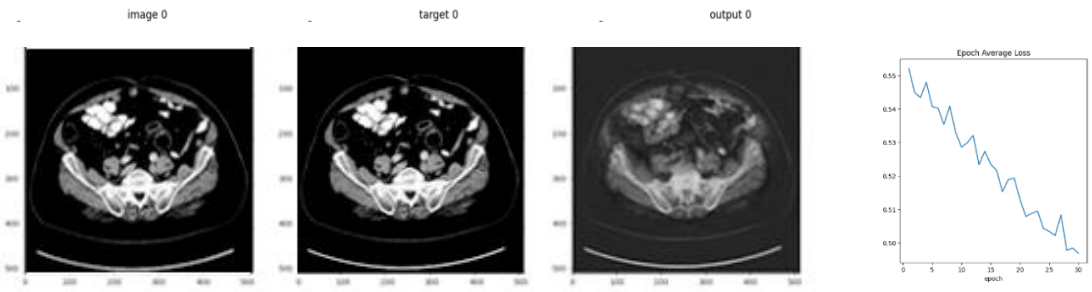

Fig 1: One slice of output and raining loss, from the left to right: input, target and output of the model.

Different Models

3D-Unet-Model

Following the initial phase, we progressed to applying the developed model to the ^{68}Ga dataset.

To adapt the model for our dataset, several transformations and optimization of hyperparameters tuned to better process the specific profiles of ^{68}Ga images. First, we checked the model just for one patient data.

Fig 2 and Table 2 in this section detail the variables and outputs from this phase of the project.

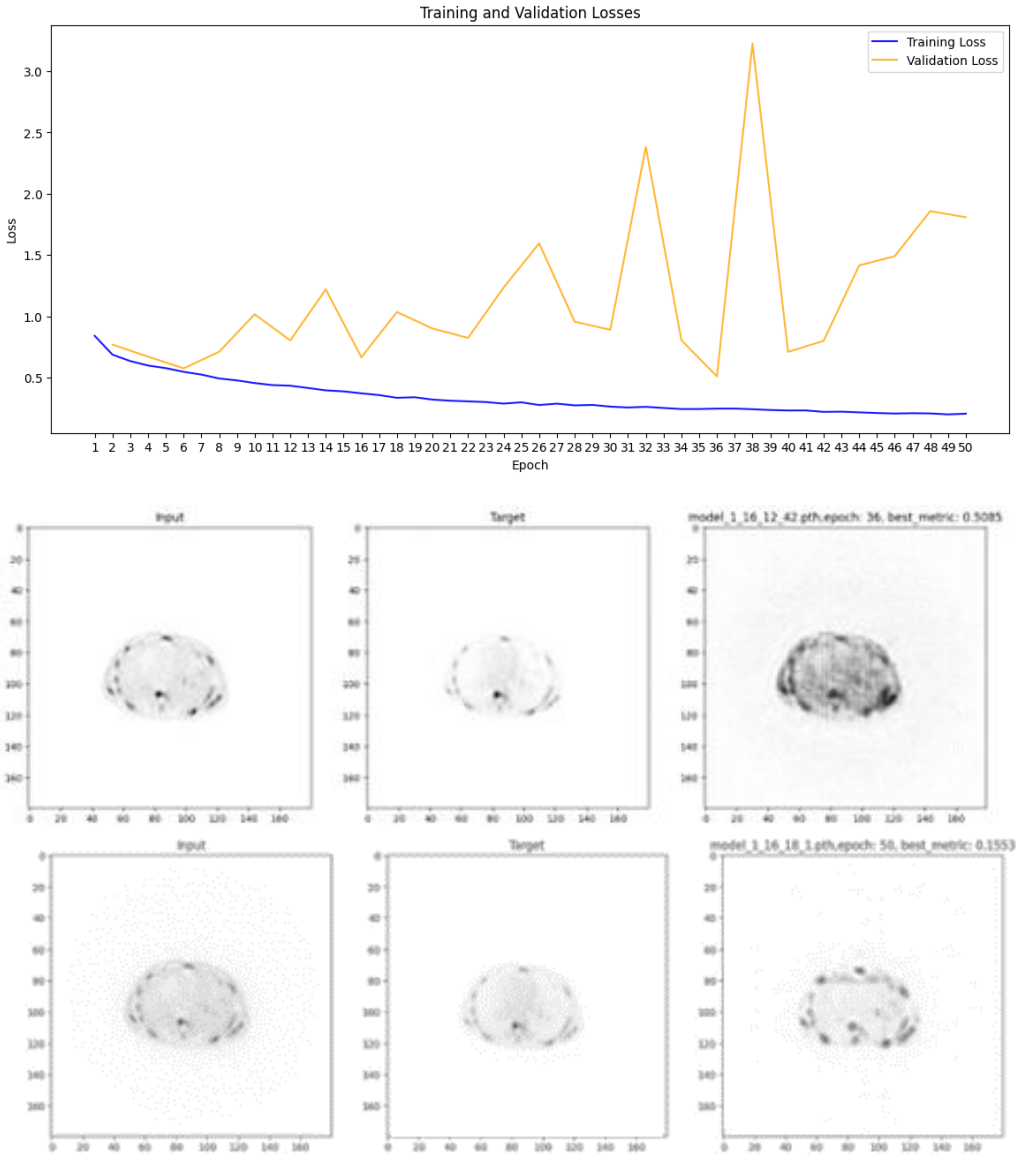

Fig 2: top: Training and validation loss for 3D-Unet model, bottom: One slice of output.And then we tried it for a portion of data (20 patient)

Table 2: Some specification of training approach

crop_size	(180, 180, 312)
train_transforms	Spacingd(keys=["image", "target"], pixdim=(1.5, 1.5, 2.0)), Resized(keys=["image", "target"], spatial_size=crop_size, ode='bilinear')
val_transforms	Spacingd(keys=["image", "target"], pixdim=(1.5, 1.5, 2.0)), Resized(keys=["image", "target"], spatial_size=crop_size, mode=('bilinear'))
batch_size	2
model	UNet(spatial_dims=3, in_channels=1, out_channels=1, channels=(16, 32, 64), act=(nn.ReLU6, {"inplace": **True**}), strides=(2, 2), num_res_units=2, norm=Norm.BATCH,
loss_function	torch.nn.MSELoss()
optimizer	torch.optim.Adam(model.parameters(), 1e-4)
max_epochs	50

As it is obvious there was still some patch pattern on the image, and it means there are parameters need to be changed.

As it is mentioned in table 3 after adapting the spacing, dimensions and other parameters for loading the data appropriate for our dataset, and using all dataset, the Fig 4 concluded.

Table 3: Some specification of training approach

roi_size	[168, 168, 320]
train_transforms	Spacingd(keys=["image", "target"], pixdim=(4.07, 4.07, 3.00)), SpatialPadd(keys=["image", "target"], spatial_size=(200, 200, 350), mode='constant'), CenterSpatialCropd(keys=["image", "target"], roi_size=roi_size),

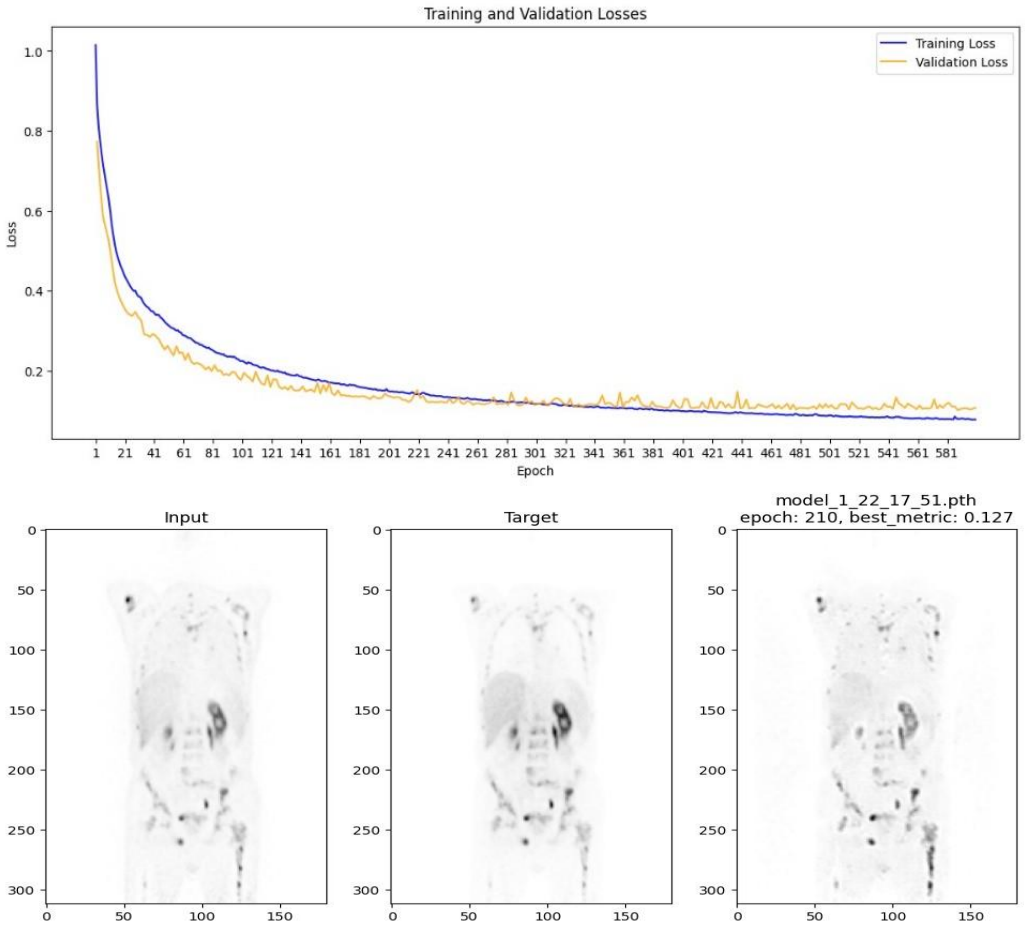

Fig 3: top: Training and validation loss for 3D-Unet model, bottom: One slice of output.

Patched-3D U-net:

In the initial phase of our research, we attempted to use full-body 3D PET data as single inputs for training our deep learning model. This approach, however, presented significant challenges. The limited number of available data and the limited computational resources required to process full-body 3D data.

Most researchers in this field typically use a 2D slice-wise approach using data-frame images, which significantly reduces the computational demand. Others utilize a smaller section of the data frame, training their models patch-wise to manage resource constraints effectively. Considering these factors, we opted to focus on using image patches exclusively in the axial direction and fixed boundaries in the coronal and sagittal dimensions 168 and 168, with each patch containing 32 axial slices. This approach effectively increased our data tenfold, facilitating more extensive training under limited resource conditions.

The outcomes of this method are presented in Fig 5 and Table 4. These results underline the adaptability of our approach in optimizing data usage and computational resources while still enabling robust model training.

Table 4: Some specification of training approach

roi_size	[168, 168, 320]
train_transforms	Spacingd(keys=["image", "target"], pixdim=(4.07, 4.07, 3.00), mode= 'trilinear'), SpatialPadd(keys=["image", "target"], spatial_size=(168, 168, 320), mode='constant'), *# Pad to ensure minimum size* RandCropByPosNegLabeld(keys=["image", "target"],label_key="target", spatial_size=(168, 168, 32), pos=1,neg=1,num_samples=4,image_key="image",image_threshold=0,
val_transforms	Spacingd(keys=["image", "target"], pixdim=(4.07, 4.07, 3.00), mode= 'trilinear'), SpatialPadd(keys=["image", "target"], spatial_size=(168, 168, 320), mode='constant'), *# Pad to ensure minimum size*
batch_size	16
model	UNet(spatial_dims=3,in_channels=1,out_channels=1, channels=(32, 64, 128, 256),act=(nn.ReLU6, {"inplace": **True**}),strides=(2, 2, 2, 2), num_res_units=2,
optimizer	torch.optim.Adam(model.parameters(), lr=1e-4, weight_decay=0.0)
scheduler	torch.optim.lr_scheduler.StepLR(optimizer, 40, 0.1)
max_epochs	150

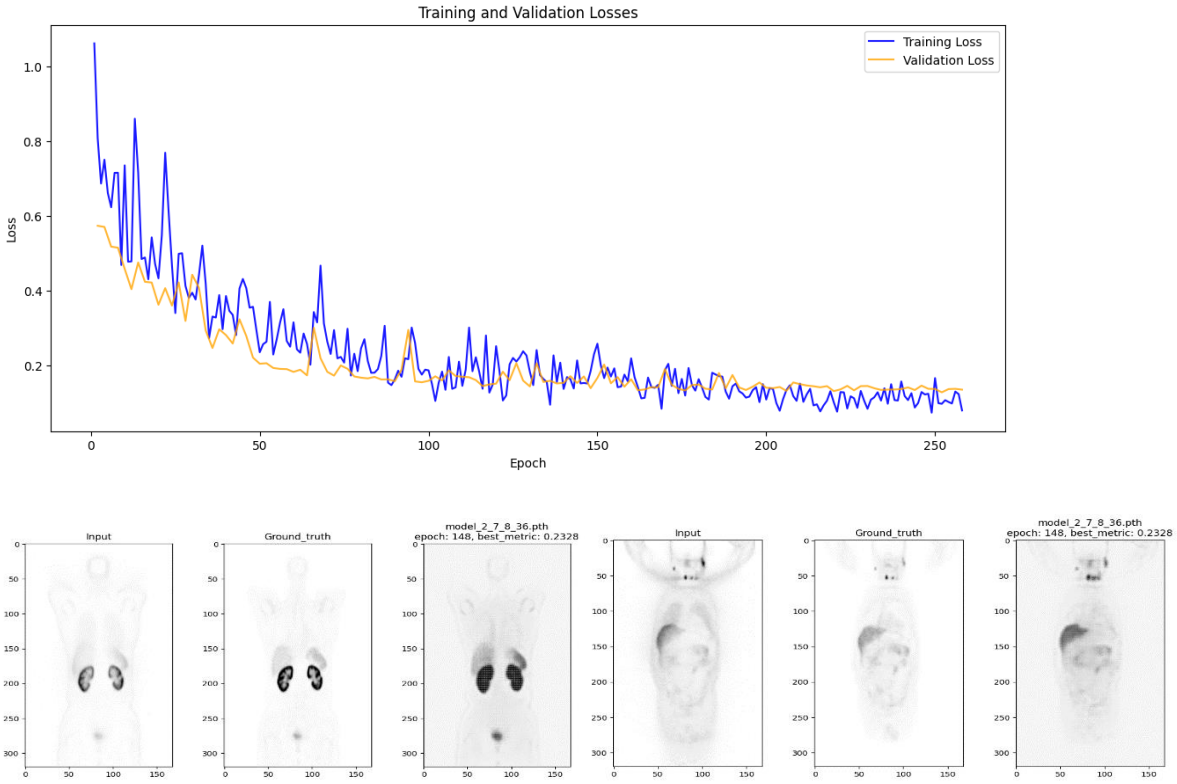

Fig 4: top: Training and validation loss for 3D-Unet model, bottom: Two sample slices of outputs, Best Metric: 0.2328, Epoch: 148

2D-Unet

In addition to search for the best match model to get lower loss and better quality of images, we evaluated a 2D-Unet model training approach.

This 2D U-Net architecture was mostly similar to the previous model. The model training was optimized using an Adam optimizer with a specifically tailored learning rate schedule, which adjusted the learning rate based on the epoch count to enhance training stability and performance.

Some key variables and results detailed in Fig 4 and Table 4.

Table 5: Some specification of training approach

train_transforms	Spacingd(keys=["image", "target"], pixdim=(4.07, 4.07), mode= 'bilinear'), spatial_size=[168, 168], mode='constant'
model	monai.networks.nets.UNet(spatial_dims=2,in_channels=1,out_channels=1,channels=(16, 32, 64, 128),strides=(2, 2, 2, 2),num_res_units=2,
loss_function	= torch.nn.MSELoss()
optimizer	torch.optim.Adam(model.parameters(), lr=learning_rate, betas=(0.5, 0.999))
max_epoch	300
lr_lambda	DecayLR(epochs=max_epochs, offset=0, decay_epochs=decay_epoch).step
scheduler	torch.optim.lr_scheduler.LambdaLR(optimizer, lr_lambda=lr_lambda)

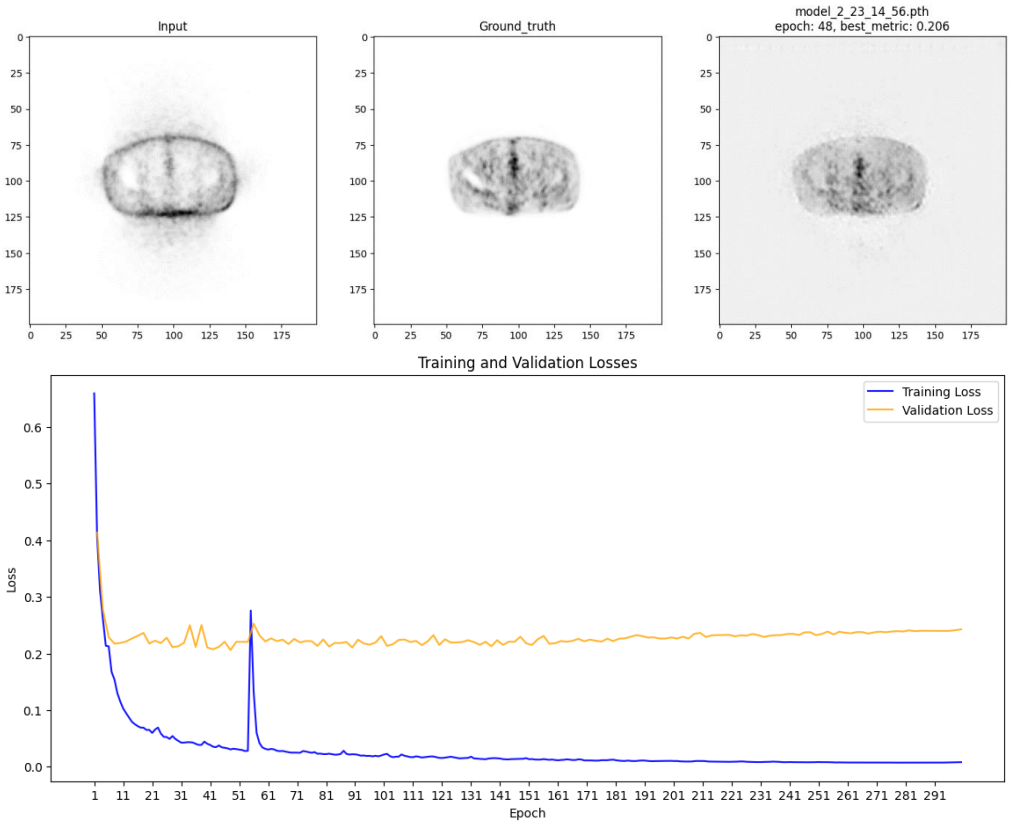

Fig 5: top: Training and validation loss for 2D-Unet model, bottom: Sample slice of output, Best Metric: 0.206, Epoch: 48

DyUnet:

In parallel with 2D evaluation, we implemented the DynUNet architecture, an advanced and dynamic variant of the traditional U-Net designed specifically for biomedical image segmentation.

DynUNet introduces several key enhancements over the standard U-Net, including the option for deep supervision. This feature allows the network to output additional intermediate layers' predictions and facilitate the learning process by ensuring that gradients are effectively propagated back through the network, enhancing the training dynamics and enabling the model to learn detailed representations without significant overfitting.

With compatible configurations of kernel sizes and strides and depth of artitecture, model enables to effectively capture relevant features at different scales.

Key configuration parameters of DynUNet are listed in table 6 and there is one sample output from out initial implementation in the Fig 5.

Table 6: Some specification of training approach

patch_size	[168, 168, 16]
spacing	[4.07, 4.07, 3.00]
spatial_size	(168, 168, 320)
train_transforms	Spacingd(keys=["image", "target"], pixdim= spacing, mode= 'trilinear'),SpatialPadd(keys=["image","target"], spatial_size=spatial_size, mode='constant'),RandSpatialCropSamplesd(keys=["image","target"], roi_size=self.patch_size, num_samples=4),
val_transforms	CenterSpatialCropd(keys=["image", "target"], roi_size=self.spatial_size)
Model	DynUNet(spatial_dims=3, in_channels=1, out_channels=1, kernel_size=kernels, strides=strides, upsample_kernel_size=strides[1:], norm_name="INSTANCE", deep_supervision=True, deep_supr_num=2,)

After these improvements, we could finally decrease the validation loss from around 0.2 at the initial trials to 0.0664. To enhance the robustness of our model, we implemented specific data augmentations. These included adding rotations of ±15 degrees and increasing the number of samples per patient from 4 to 20.

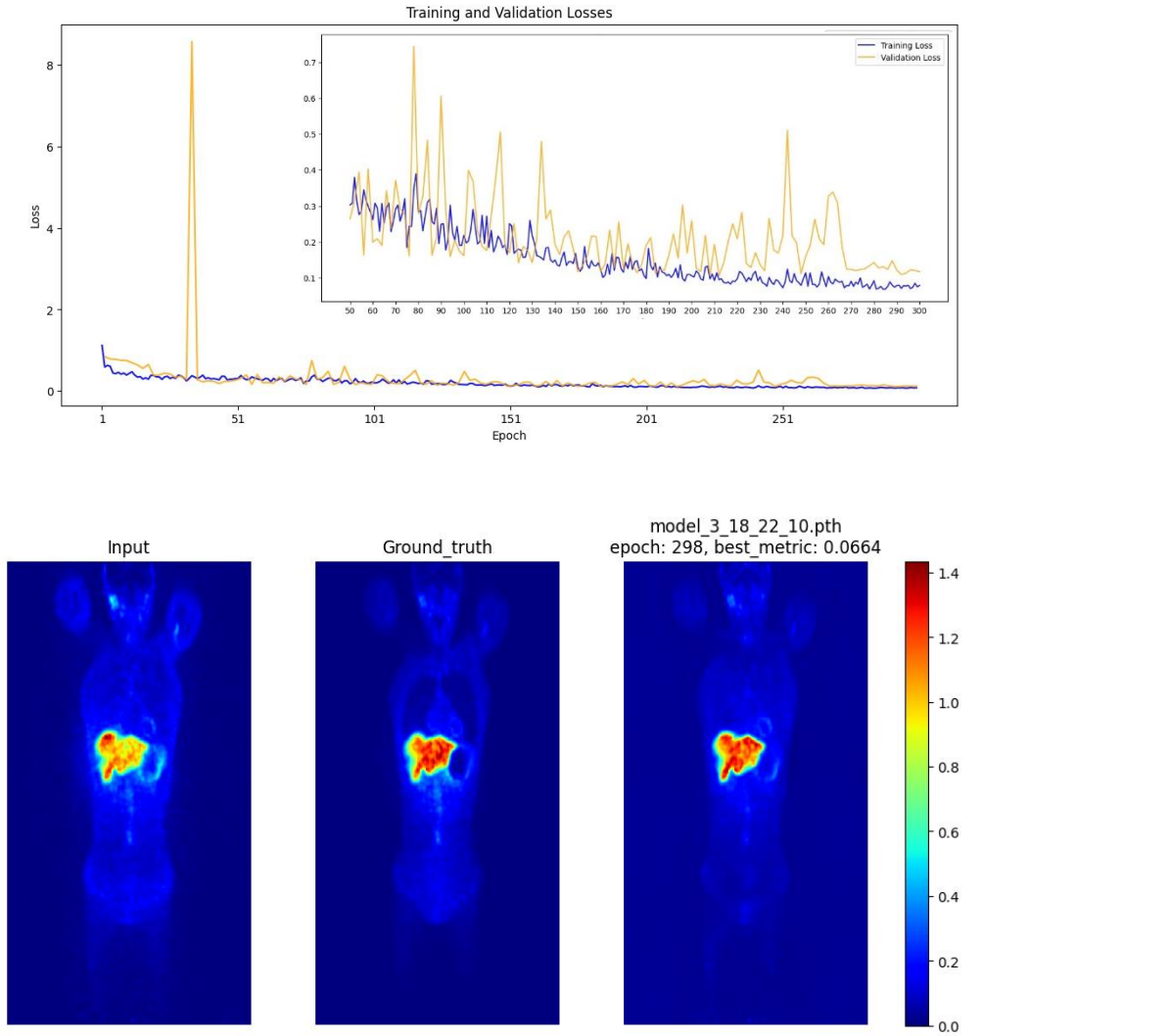

Fig 6: top: Training and validation loss for 2D-Unet model, bottom: Sample slice of output, Best Metric: 0.206, Epoch: 48

Here are some other metric errors from the beginning of this research:

At early stage	ME: 0.64 MAE: 0.95 RE: 193.7% ARE: 199.0%
Using Unet	Mean Error (SUV): -0.32 ± 0.1032 Mean Absolure Error (SUV): 0.33 ± 0.0868 Relative Error (SUV%): -55.49 ± 15.6193 Absolure Relative Error (SUV%): 56.98 ± 13.3306 Root Mean Squared Error: 0.48 ± 0.1741 Peak Signal-to-Noise Ratio: 23.92 ± 6.4356 Structual Similarity Index: 0.63 ± 0.1537
Using DynUnet	mean_error: -0.43 ± 0.3433 mean_absolute_error: 0.54 ± 0.2896 relative_error: -23.92 ± 14.8091 absolute_relative_error: 35.36 ± 7.7831 rmse: 1.13 ± 0.8008 psnr: 32.57 ± 4.2616 ssim: 0.87 ± 0.0568
DynUnet, ADCM method	Mean Error (SUV): -0.42 ± 0.0783 Mean Absolure Error (SUV): 0.42 ± 0.0767 Relative Error (SUV%): -72.41 ± 10.2247 Absolure Relative Error (SUV%): 72.65 ± 9.9125 Root Mean Squared Error: 0.57 ± 0.1856 Peak Signal-to-Noise Ratio: 22.53 ± 6.7792 Structual Similarity Index: 0.44 ± 0.1617

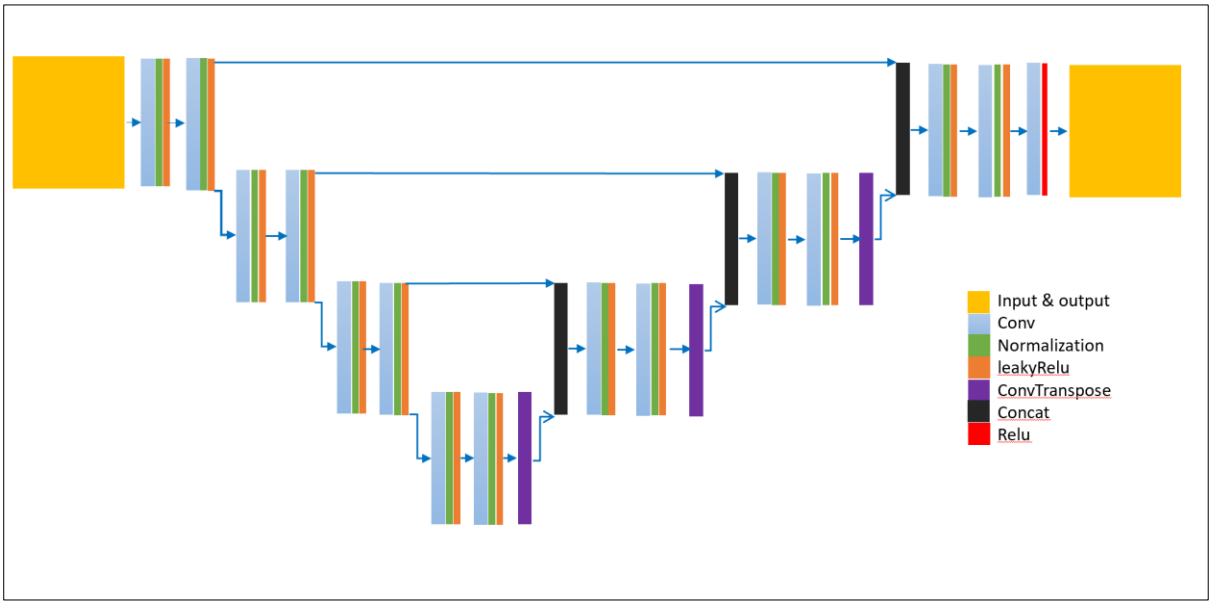

Fig 7: The architecture of DynUnet.

Supplementary Material 2

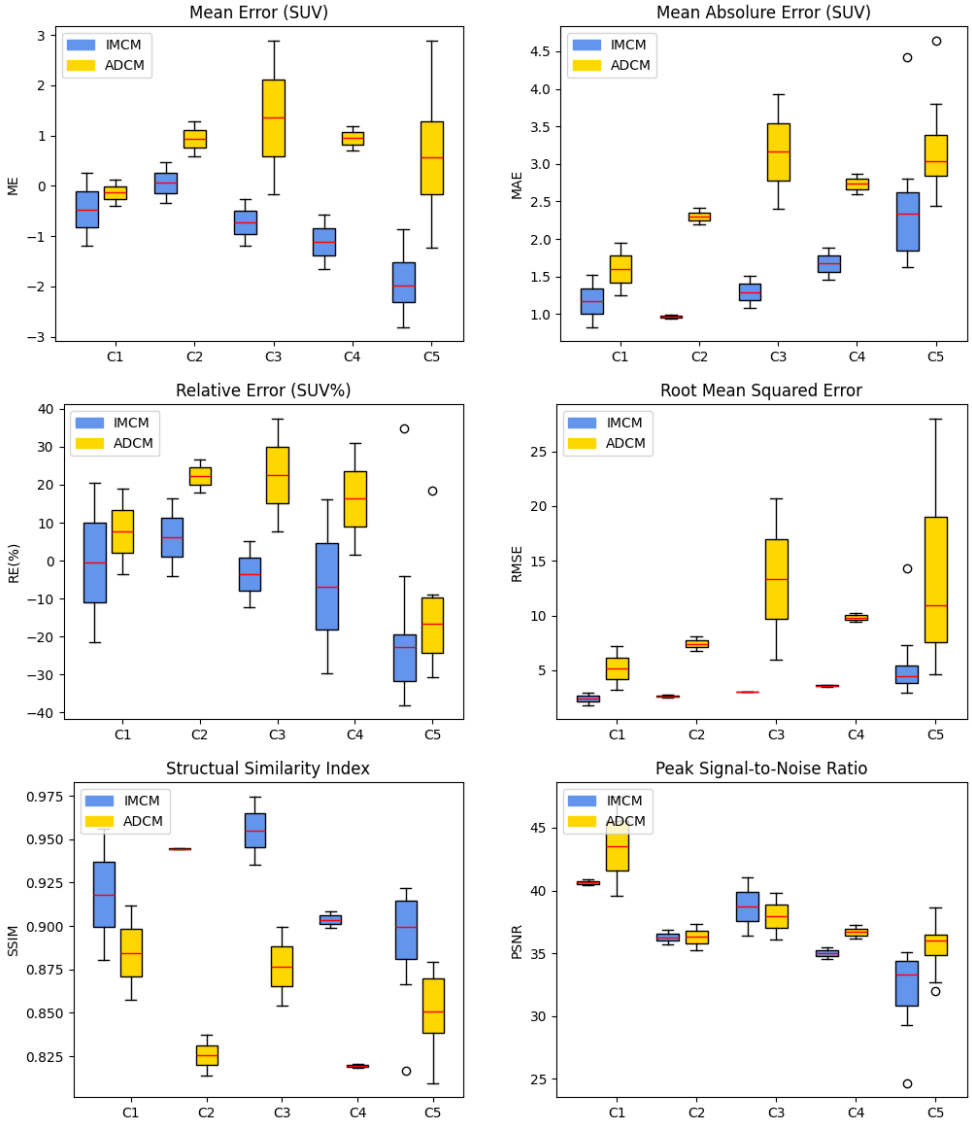

Fig 7: Performance Metrics of IMCM and ADCM Across Centers C1 to C5

Table 7: Summary statistics of quantitative parameters for different approaches on cross center (Ga dataset)

	Method	ME	MAE	RE	ARE	RMSE	PSNR	SSI
Mean ± SD	**ADCM**	0.67 ± 1.10	2.87 ± 0.75	-2.17 ± 20.85	57.23 ± 7.41	11.79 ± 7.03	36.83 ± 3.17	0.85 ± 0.03
	IMCM	-1.38 ± 0.93	1.94 ± 0.83	-12.38 ± 20.98	43.62 ± 11.56	4.40 ± 2.66	34.42 ± 3.92	0.91 ± 0.04
CI95%	**ADCM**	[0.15, 1.18]	[2.52, 3.22]	[-11.93, 7.59]	[53.77, 60.70]	[8.50, 15.08]	[35.35, 38.31]	[0.84, 0.86]
	IMCM	[-1.81, -0.94]	[1.55, 2.33]	[-22.20, -2.56]	[38.21, 49.04]	[3.16, 5.65]	[32.58, 36.25]	[0.89, 0.92]

Statistical tests

Normality Testing

Before selecting an appropriate statistical test for our analysis, we first assessed the normality of the distribution of each metric within both datasets using the Shapiro-Wilk test. This step was crucial to determine whether parametric or non-parametric statistical methods were suitable. Our findings indicated that several metrics did not follow a normal distribution, particularly in the IMCM dataset, where metrics such as Relative Error (SUV%) and Absolute Relative Error (SUV%) showed significant deviations from normality with p-values below 0.05. Similarly, Root Mean Squared Error and Peak Signal-to-Noise Ratio in the ADCM dataset also deviated significantly from a normal distribution.

Table 8: Evaluation of normality of all metric variables across both ADCM and IMCM datasets by performing a Shapiro-Wilk test for each metric.

	Metric	ADCM Statistic	ADCM P-value	IMCM Statistic	IMCM P-value
0	Mean Error (SUV)	0.962684	0.598745	0.964505	0.637189
1	Mean Absolure Error (SUV)	0.973161	0.819726	0.902938	0.046832
2	Relative Error (SUV%)	0.926644	0.133062	0.903215	0.047397
3	Absolure Relative Error (SUV%)	0.934748	0.190480	0.813324	0.001375
4	Root Mean Squared Error	0.875041	0.014425	0.670732	0.000018
5	Peak Signal-to-Noise Ratio	0.826691	0.002222	0.944862	0.295736
6	Structual Similarity Index	0.963606	0.618108	0.973200	0.820480

Choice of Statistical Test

Given the non-normality observed in several key metrics across the datasets, we opted to use the Wilcoxon signed-rank test, a non-parametric method, for our analysis. This test is particularly advantageous as it does not assume the normality of the data and is ideal for comparing two related samples or repeated measurements on a single sample. This choice was reinforced by the need to handle the paired nature of our data, where each center was analyzed under both ADCM and IMCM conditions.

Our analysis revealed significant differences in several metrics between the ADCM and IMCM methodologies. Notably, the Mean Error (SUV) and Absolute Relative Error (SUV%) showed considerable variations, suggesting distinct impacts of the two methodologies on these particular metrics. The Wilcoxon test results indicated statistically significant differences with low p-values, underscoring the effectiveness of one method over the other in specific conditions.

Table 9: Summarized results of the Wilcoxon test with the False Discovery Rate (FDR) corrections applied to the p-values.

Metric	U-statistic	P-value
Mean Error (SUV)	371.0	0.000039
Mean Absolute Error (SUV)	330.0	0.000460
Relative Error (SUV%)	267.0	0.072045
Absolute Relative Error (SUV%)	357.0	0.000023
Root Mean Squared Error	364.0	0.000097
Peak Signal-to-Noise Ratio	286.0	0.020734
Structural Similarity Index	42.0	0.000020

The results from the Wilcoxon test show that there are statistically significant differences between the ADCM and IMCM datasets for most of the image-derived metrics, except for the "Relative Error (SUV%)" where the corrected p-value does not indicate a statistically significant difference.

Table 10: Summary statistics of quantitative parameters for different approaches on cross tracer (FDG dataset)

	Method	ME	MAE	RE	ARE	RMSE	PSNR	SSI
Mean ± SD	**ADCM**	0.29 ± 0.58	1.08 ± 0.35	34.08 ± 48.96	80.22 ± 34.25	3.71 ± 4.14	37.38 ± 3.89	0.77 ± 0.09
	TL-MC	-0.54 ± 0.15	0.69 ± 0.13	-39.70 ± 9.13	52.11 ± 7.61	1.18 ± 0.61	35.27 ± 6.18	0.78 ± 0.11
CI95%	**ADCM**	[0.02, 0.55]	[0.92, 1.24]	[11.80, 56.37]	[64.63, 95.81]	[1.82, 5.59]	[35.61, 39.15]	[0.72, 0.81]
	TL-MC	[-0.60, -0.47]	[0.63, 0.75]	[-43.86, -35.55]	[48.64, 55.57]	[0.91, 1.46]	[32.46, 38.09]	[0.73, 0.83]

Table 11: Summary statistics of quantitative parameters for different centers tuned for each radiotracer separately (TL-MC) and tested on all test sets (centers 1-7).

Quantitative metric	Center 1-4	Center 5	Center 6	Center 7	All Test Set
ME	-0.56 ± 0.74	-1.92 ± 0.58	-0.46 ± 0.16	-0.61 ± 0.09	-0.95 ± 0.78
MAE	1.28 ± 0.37	2.38 ± 0.76	0.64 ± 0.13	0.73 ± 0.12	1.30 ± 0.86
RE	-1.15 ± 18.77	-19.87 ± 19.58	-35.66 ± 11.69	-43.38 ± 3.55	-26.38 ± 21.03
ARE	36.38 ± 7.12	48.45 ± 11.62	49.56 ± 8.11	54.42 ± 6.64	47.97 ± 10.53
RMSE	2.90 ± 0.58	5.41 ± 3.05	1.00 ± 0.25	1.35 ± 0.78	2.75 ± 2.49
PSNR	37.66 ± 2.67	32.25 ± 3.04	37.74 ± 6.59	33.03 ± 5.07	34.86 ± 5.16
SSIM	0.93 ± 0.03	0.89 ± 0.03	0.80 ± 0.13	0.76 ± 0.092	0.84 ± 0.11
			CI 95%		
ME	[-1.18, 0.06]	[-2.29, -1.56]	[-0.57, -0.34]	[-0.67, -0.55]	[-1.19, -0.70]
MAE	[0.97, 1.59]	[1.90, 2.87]	[0.55, 0.73]	[0.65, 0.81]	[1.03, 1.57]
RE	[-16.84, 14.55]	[-32.31, -7.43]	[-44.02, -27.29]	[-45.77, -41.00]	[-33.01, -19.74]
ARE	[30.42, 42.34]	[41.07, 55.84]	[43.75, 55.37]	[49.96, 58.89]	[44.65, 51.29]
RMSE	[2.42, 3.38]	[3.47, 7.35]	[0.82, 1.18]	[0.83, 1.88]	[1.97, 3.54]
PSNR	[35.43, 39.90]	[30.32, 34.18]	[37.62, 37.85]	32.97 to 33.09	[33.23, 36.48]
SSIM	[0.90, 0.96]	[0.87, 0.91]	0.68 to 0.91	0.70 to 0.82	[0.81, 0.87]
Column “Center 1-4” represents the results of testing on the whole test set when training is performed on center 1 to 4 data set. “Center 5” represents as external center with same radiotracer and Center 6 & 7 test sets represent the results of tuned models, in which training and testing are performed for different radiotracer (whole 20% of the clean dataset).					